

August 1984

NASA-TP-2339 19840023279

Empirical Relations for Cavitation and Liquid Impingement Erosion Processes

P. Veerabhadra Rao
and Donald H. Buckley

11 JAN 1985

11 JAN 1985

NASA
Technical
Paper
2339

1984

Empirical Relations for Cavitation and Liquid Impingement Erosion Processes

P. Veerabhadra Rao
and Donald H. Buckley

Lewis Research Center
Cleveland, Ohio



National Aeronautics
and Space Administration

Scientific and Technical
Information Branch

Summary

Several attempts have been made in the past to predict erosion due to cavitation and liquid impingement. Most of the models and formulations suffer certain deficiencies so they do not adequately predict the magnitude of erosion, particularly during the acceleration period and for long-term exposures. This report presents a power-law relationship between average erosion rate and cumulative erosion during the acceleration and deceleration periods of erosion. A power-law relation was observed for copper, brass, and stainless steel specimens examined in a rotating disk device. Data analyses from other types of erosion devices, including venturi, magnetostriction, and liquid jet impingement, conform to the present unified relation. This agreement is indicative of the similar nature of erosion in the acceleration zone. Attempts are made to understand the relationship between the coefficients in the power-law relation and material properties.

Symbols

A	coefficient (eq. (1)), $\text{mm}^{3(1-n)}/\text{sec}$
B	coefficient (eq. (4)), $\text{mm}^{3(1+m)}/\text{sec}$
D_1	constant
m	exponent (eq. (4))
n	exponent (eq. (1))
nI	exponent (eq. (3))
p	pressure
p_1, p_2, p_3	exponents
R	correlation coefficient
t	exposure time
V	velocity
V	cumulative erosion loss
ϵ	erosion rate
Subscripts:	
a	average
i	instantaneous
ma	maximum of average erosion rate
mi	maximum of instantaneous erosion rate
peak	peak

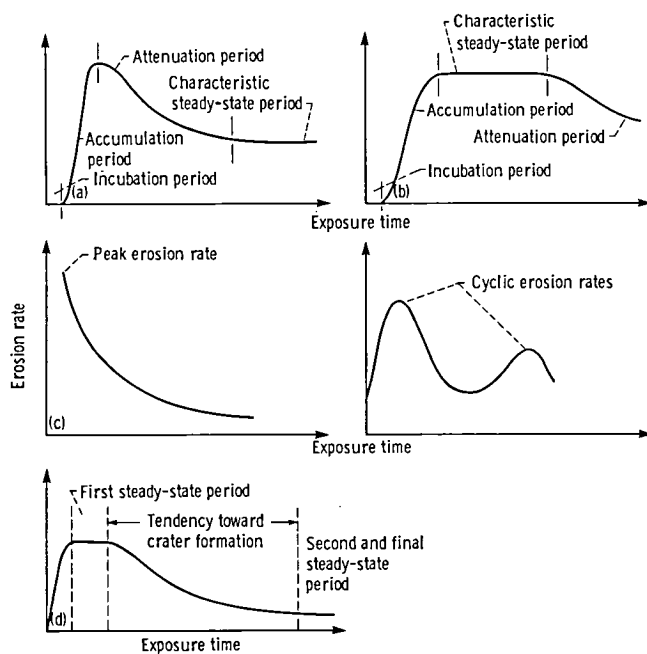
Introduction

Prediction of erosion due to cavitation and liquid impingement has been difficult in light of different instantaneous¹ erosion rate versus time curves as schematically presented in figure 1 (refs. 1 to 4). Each curve in figure 1 is a typical shape due to the experimental conditions involved, and there appears to be no direct relation between any two of them. Hence, the individual investigators attempted different ways to predict erosion rates. Thus, for predictions of short-term erosion behavior of the cavitation (refs. 5 to 7) and liquid impingement (refs. 8 to 11) erosion processes, several details such as empirical relationships between erosion rates and material properties were discussed. On the other hand, predictive attempts for long-term cavitation (refs. 3, 4, and 12 to 16) and liquid impact (refs. 3, 10, and 16 to 18) erosion have been reported. During the last several years, several plots (refs. 3 and 13), models (refs. 3, 4, 13, 15, and 18), charts (refs. 10, 12 to 16), and curve-fit approaches (refs. 17 to 19) have been reported. One recent attempt (ref. 19) indicates that an average² erosion rate versus time curve was a better way to present data and to normalize all types of irregular instantaneous erosion rate versus time curves (in fig. 1) to a smooth, regular shape.

The correlations of erosion rates with mechanical properties estimate erosion rates on an empirical basis with a least-squares-fit. In general, this approach predicts only maximum erosion rate (fig. 1(a)) or steady-state erosion rate (fig. 1(b)) from an instantaneous erosion rate versus time curve (ref. 20). For mathematical and other modeling efforts two general approaches have been used. The first group concentrated mainly on energy considerations (refs. 21 and 22), and the second group considered the typical shape of erosion versus time curve (generally S-shaped) (refs. 4, 13, 18, and 23). The latter studies were justified on the basis that advanced stages of erosion involve the interaction of local fluid flow apart from pure energy transfer and the absorption characteristics of materials. Several researchers (refs. 3,

¹Instantaneous erosion rate is calculated as the slope of the local tangent.

²Average erosion rate is calculated as the slope of total volume loss during the entire test duration.



- (a) Thiruvengadam and Preiser (magnetostriction device) (ref. 1).
 (b) Plesset and Devine (magnetostriction device) (ref. 2).
 (c) Heymann (liquid impact device) (ref. 3).
 (d) Tichler and de Gee (magnetostriction device) (ref. 4).

Figure 1. – Characteristic erosion rate as function of time curves.

4, 12 to 15, and 17 to 19) have attempted to predict long-term erosion rates.

The method proposed in reference 19 has contributed to an understanding of the universal nature of presenting erosion curves and has improved prediction ability. In addition, the method has helped in relating the similarities of erosion processes in different cavitation devices as well as between cavitation and liquid impingement erosion. Despite these improvements, the prediction ability is still limited, especially with regard to predictions for long-term operations and during the acceleration stage of the erosion process.

Some investigators have employed the average erosion rate versus cumulative erosion curves for comparison and modeling efforts using a rotating disk device (ref. 23). However, the different features of these curves have not been fully investigated. Further work is needed (1) to investigate the effect of the surface history on damage and the erosion processes associated with different devices and (2) to assess the characterization and correlation of different materials.

The objective of this report is to show a power-law relation between average erosion rate and cumulative erosion during the acceleration and deceleration zones of the erosion process. Further, it was found that erosion results with other types of erosion devices—including magnetostriction, venturi, and liquid impingement devices—conform to this type of formulation and relation during the acceleration zone.

Experimental Device and Test Conditions

The rotating disk device (fig. 2) consists of a cast-iron chamber in which a 330-mm-diameter metallic disk rotates. The chamber has eight sets of radial baffles spaced at equiangular distances on either side of the disk to prevent the circulation of water contained in the chamber. The clear distances from the disk to the front and rear baffles are 10.4 and 5 mm, respectively. The chamber is connected to an overhead water tank. The inlet and outlet valves provided for the chamber are used for regulating pressure and temperature in the chamber. The front side of the chamber has a transparent cover to enable visual observation of the cavity shapes with the aid of a stroboscopic lamp. The metallic disk consists of a 1.5-mm-thick mild steel base sheet over which a 3-mm-thick aluminum face sheet is screwed. Six diametrically opposite grooves (64 mm in diameter) are cut in the face sheet to fix circular test specimens (63.5 mm in diameter). Cavitation is induced by 25.4-mm-diameter, 3-mm-thick bodies mounted over the disk. The details of the rotating disk used in the experiments are presented in figure 2.

The static pressure in the chamber was varied from 0.11 to 0.16 MPa (absolute). The pressure in the chamber was measured with a U-tube manometer. The velocities varied from 35 to 37.3 m/sec. The rotational frequency of the motor was kept at 48.75 Hz (2925 rpm). All the experiments were conducted with test specimens 63.5 mm in diameter from different materials and with cavitation inducers 25.4 mm in diameter, 3 mm thick, and made of yellow brass. The average ambient temperature of the test water was $34 \pm 2^\circ \text{C}$.

The test duration on different materials was varied depending on the cumulative erosion obtained. The test specimens were weighed with a balance of 200-g capacity and 0.1-mg sensitivity. The specimens were thoroughly washed with distilled water and then alcohol, dried with a hair drier, and kept in a desiccator for 4 hr before each weighing. No other pretest treatment was done. The volume of erosion was calculated as the ratio of weight loss to the density of the material. Three specimens were tested at each velocity and pressure, and the average weight loss was taken. Specimens were prepared from 3-mm-thick sheet that was free of surface scratches. The mechanical properties of the materials used and their chemical compositions are given in references 19 and 24.

Data Presentation

Empirical Power-Law Relationships

Figure 3 presents a typical set of plots of average erosion rate (total volume loss/total exposure time) versus volume loss of different materials tested in the

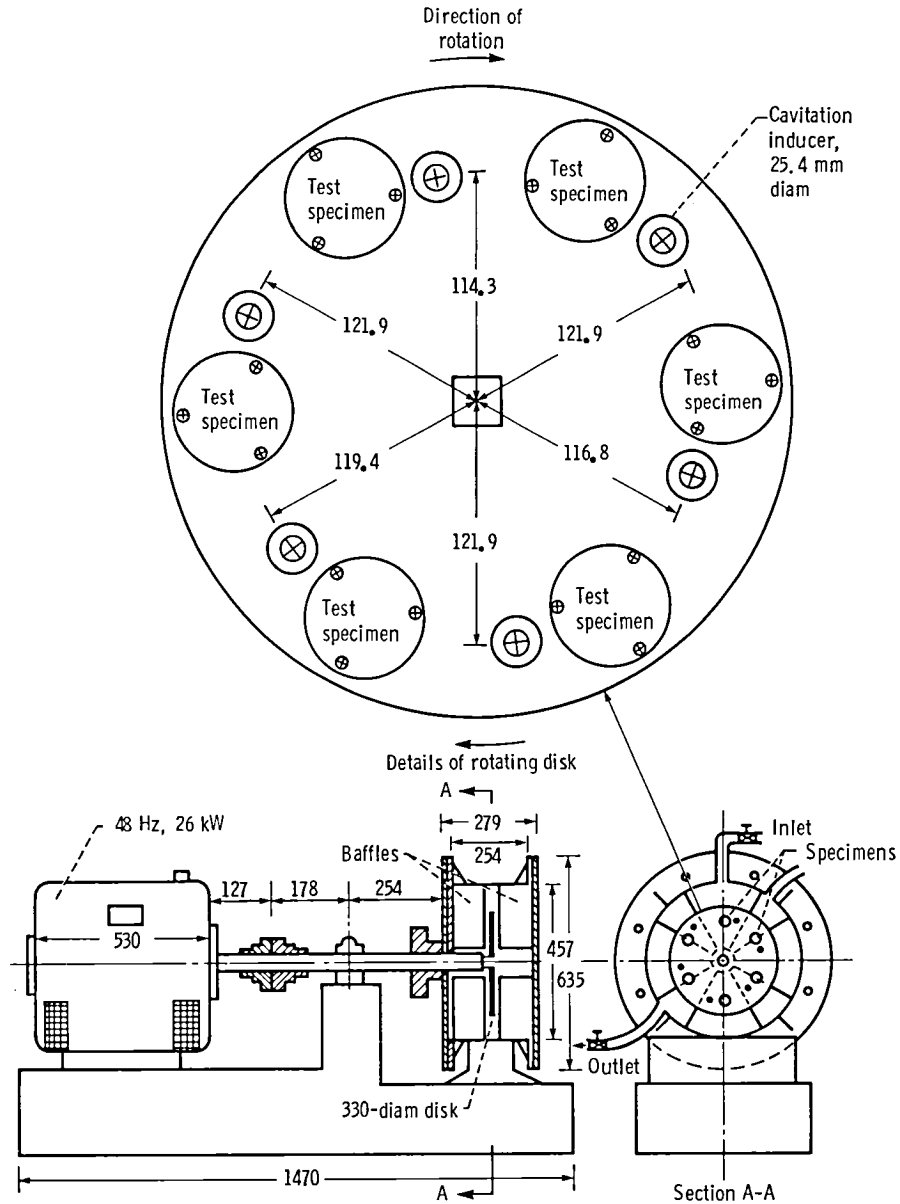


Figure 2. – Sectional views of rotating-disk device. (All dimensions are in mm.)

rotating disk device. The experimental conditions are a pressure (absolute) of 0.15 MPa and a velocity of 37.3 m/sec. It appears that the curves in figure 3 have acceleration, either a plateau (steady-state) or a peak, and deceleration zones. The experimental points can be represented by power-law relationships. The equation for the acceleration zone is written as

$$V/t = A V^n \quad (1)$$

or

$$V = (At)^{1/(1-n)} \quad (2)$$

where V is the cumulative volume loss (in mm^3), t the

exposure time corresponding to V (in min or hr), A a constant depending on the material, and n an empirically determined exponent. Differentiation of equation (2) with respect to t yields

$$dV/dt = A V^n / (1-n) = V / [(1-n)t] = D_1 t^{n_1} \quad (3)$$

where

$$D_1 = A^{1/(1-n)} / (1-n)$$

$$n_1 = n / (1-n)$$

Similarly, the equation for the deceleration zone (following the peak) is represented as

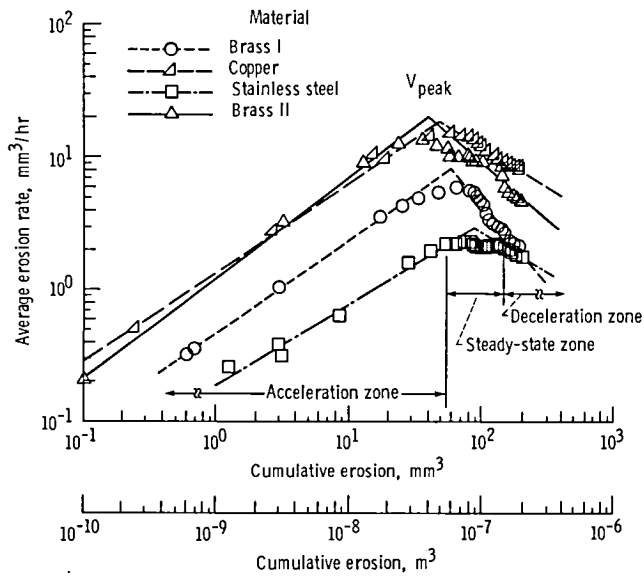


Figure 3. — Average erosion rate as function of erosion progression in a rotating disk device. Flow velocity, V , 37.3 m/sec; pressure, p , 0.15 MPa (abs); test liquid, tap water; cavitation number, 0.21.

$$V/t = BV^{-m} \quad (4)$$

or

$$V = (Bt)^{1/(1+m)} \quad (5)$$

where B and m are empirical constants to be determined from data analysis. Differentiating equation (5) with respect to t gives

$$dV/dt = V/[(1+m)t] \quad (6)$$

$$= B^{1/(1+m)} t^{-m/(1+m)} / (1+m) = D_2 t^{n_2} \quad (7)$$

The coefficients, exponents, and correlation coefficients obtained by the least-squares fit of the experimental data points in figure 3 are presented in table I. (All tables appear at the end of the report, pp. 19–24.) Table I also presents peak (maximum) average erosion rates, cumulative erosion, time to attain the peak rate, peak (maximum) instantaneous erosion rate, cumulative erosion, and time to attain the peak. Equations (3) and (6) indicate that the instantaneous erosion rate dV/dt within these two zones is always a function of the cumulative average erosion rate V/t . The ratios of these two rates are constant. The intersection point for these two lines may be obtained by equating equations (1) and (4):

$$AV^n = BV^{-m} \quad (8)$$

or

$$V = (B/A)^{1/(n+m)} \quad (9)$$

The value of V in equation (9) corresponds to the maximum of the average erosion rate versus erosion curve and the maximum values of V/t , and the time corresponding to this peak may be obtained by using either equation (1) or (4).

From this study it appears that (1) exponents n and m are almost equal (in cases where values are available, table I), (2) a power-law relation exists between instantaneous erosion rate and exposure time (eqs. (3) and (7)), and (3) with a few experimental data points the curves can be fitted. The experimental observations actually deviate from the assumed relationship (eq. (1)) at the maximum value of dV/dt . Also, the experimental data points always fall below the assumed relation of equation (1).

Figures 4 to 6 present average erosion rate versus erosion for different materials tested in a rotating disk device at different velocities (ref. 24). Table I further presents data pertaining to the ratio of $\epsilon_{ma}/\epsilon_{mi}$ and $(1-n)$ where $\epsilon_{ma} = (V/t)_{\max}$ and $\epsilon_{mi} = (dV/dt)_{\max}$. The disagreement of these two values indicates the degree to which the experimental data deviate from the empirical power-law relationship. At any cumulative erosion it is observed that the values of the coefficients for different materials decrease as the erosion rates decrease. Exponents do not, however, show a clear trend.

Discussion

It is logical to assume that the instantaneous erosion rate is always dependent on some measure of the surface condition such as mean depth of penetration (MDP),

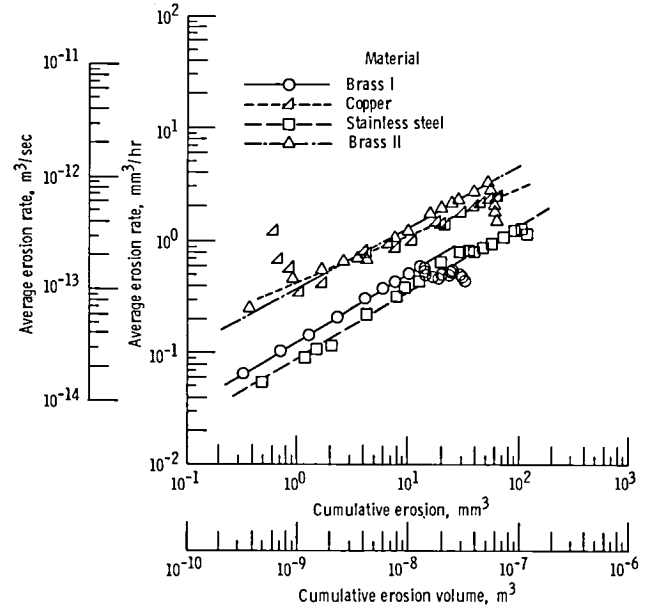


Figure 4. — Average erosion rate as function of erosion progression in a rotating disk device. Flow velocity V , 36.6 m/sec; pressure, p , 0.15 MPa (abs); test liquid, tap water; cavitation number, 0.22.

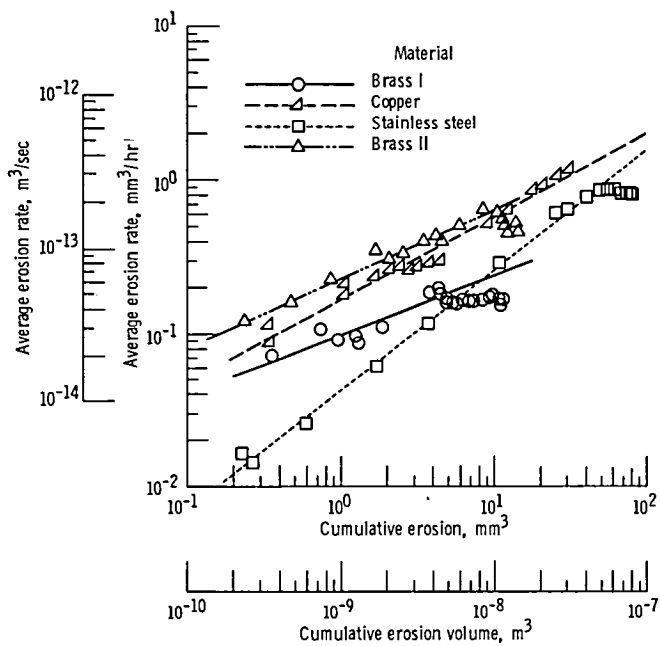


Figure 5. — Average erosion rate as function of erosion progression in a rotating disk device. Flow velocity, V , 35.8 m/sec; pressure, p , 0.15 MPa (abs); test liquid, tap water; cavitation number, 0.23.

cumulative volume loss, or roughness. At the same time, it is known that the flow pattern changes due to cumulative erosion, and this will affect the erosion process for all types of experimental devices.

In common engineering flow systems, cavitation bubbles form in low-pressure regions and collapse close to a material wall. As a result, a high-velocity liquid microjet is formed because of a highly asymmetric collapse process. It was generally observed that a rigid surface³ attracts the bubble centroid during collapse and results in microjet generation toward the wall (ref. 26) causing damage on the surface. It was further noticed that *only one* out of a very large number of bubbles ($N \sim 10^4$ to 10^9), observed to collapse near a surface by high-speed photography, actually produces a detectable crater. Plesset and Chapman (ref. 27) and Lauterborn and Bolle (ref. 28) estimate microjet velocities of 130 and 170 m/sec for two typical cases with water as the test liquid. On the other hand, Brunton (ref. 29) estimates a possible microjet velocity of up to 1000 m/sec. Photographic observations (ref. 30) indicate $\sim 80\text{-}\mu\text{m}$ -diameter and ~ 100 m/sec-velocity microjets for an initial bubble diameter of 4 mm. The stress pulse time is $0.1\text{ }\mu\text{sec}$, indicating very high strain rates during the cavitation erosion process.

³Asymmetric collapse at a sufficiently flexible surface or a free surface reverses the collapse direction and results in the repulsion of the bubble centroid from the surface and the generation of the microjet away from the surface (ref. 25).

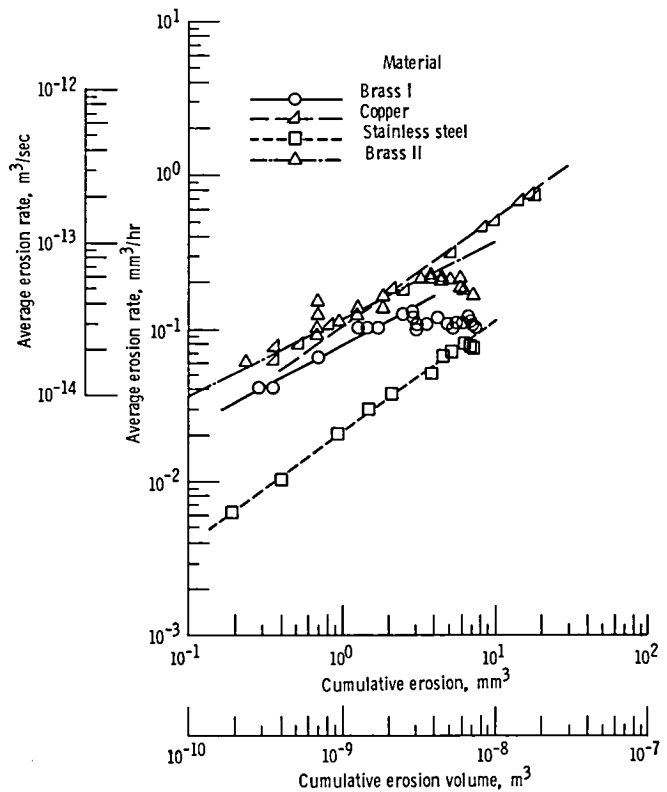
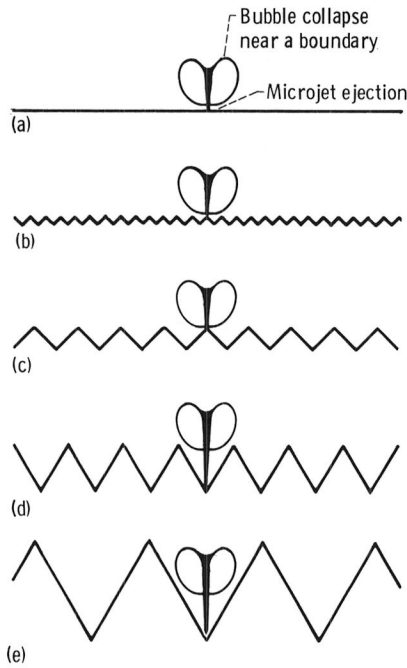


Figure 6. — Average erosion rate as function of erosion progression in a rotating disk device. Flow velocity, V , 35 m/sec; pressure, p , 0.15 MPa (abs); test liquid, tap water; cavitation number, 0.24.

Figure 7 presents schematic diagrams representing the progression of erosion and surface roughness with time. The individual pits caused by microjets initiate cumulative erosion on the surface, and plastic deformation, flow, fatigue- or ductile-type failure, and final material loss result. The surface roughness may increase to a steady-state value (fig. 7(d)) at which point the microjets generally become less effective in causing damage and erosion to the surface. The damage, however, continues at a decreased pace but does not cease. These two regions may possibly be identified as steady-state and deceleration zones in figure 3.

Figure 8 presents available micrographs of the erosion progression with respect to time for an aluminum specimen examined in a rotating disk device (ref. 24) in the deceleration zone. The photographs in figure 8 show an increase in the area of erosion more than the depth of erosion supporting the schematic representation of figure 7. Apart from this observation the following observations by different investigators also support the present postulations pertaining to the acceleration, steady-state, and deceleration zones.

The information on bubble dynamics in a rotating disk or venturi device with respect to the progression of erosion is available (refs. 24 and 31 to 34). Cavity size and number of bubbles increase as the erosion process



(a) Initial flat surface.
 (b) Inception (of impacts) roughness.
 (c) Developed roughness.
 (d) Inception of steady-state roughness.
 (e) Fully developed roughness resulting in deceleration roughness and erosion. Efficiency of microjet damage reduced.

Figure 7.—Schematic representation of microjet impact as function of exposure time.

progresses. This corresponds to the acceleration zone shown in figure 3 where both area and depth of erosion increase. Once the area of erosion stabilizes, only depth of erosion increases, resulting in a steady-state zone. Some of these concepts were discussed earlier (refs. 24 and 35).

When the erosion is fully developed, the cavity size continues to increase, but the number of bubbles appears to decrease. This corresponds to the deceleration zone. The postulation of number of bubbles decreasing as the erosion increases is shown in figure 9. The individual bubbles have enormous damaging energy as observed in the literature (ref. 6). As the depth of erosion becomes large, the eroded area traps cavitation bubbles, as shown in figure 7(e) and as was observed with magnetostriction devices (refs. 2,4, 20), and reduces the erosion rate, possibly due to compressibility and cushioning effects, resulting in the deceleration zone.

Despite the fact that m and n are equal in the majority of cases, some deviations are noticed (see figs. 3 to 6 and table I). These differences may be a result of the gross erosion change on the specimen, due to the removal of large pieces of material, erosion at an edge, hole piercing

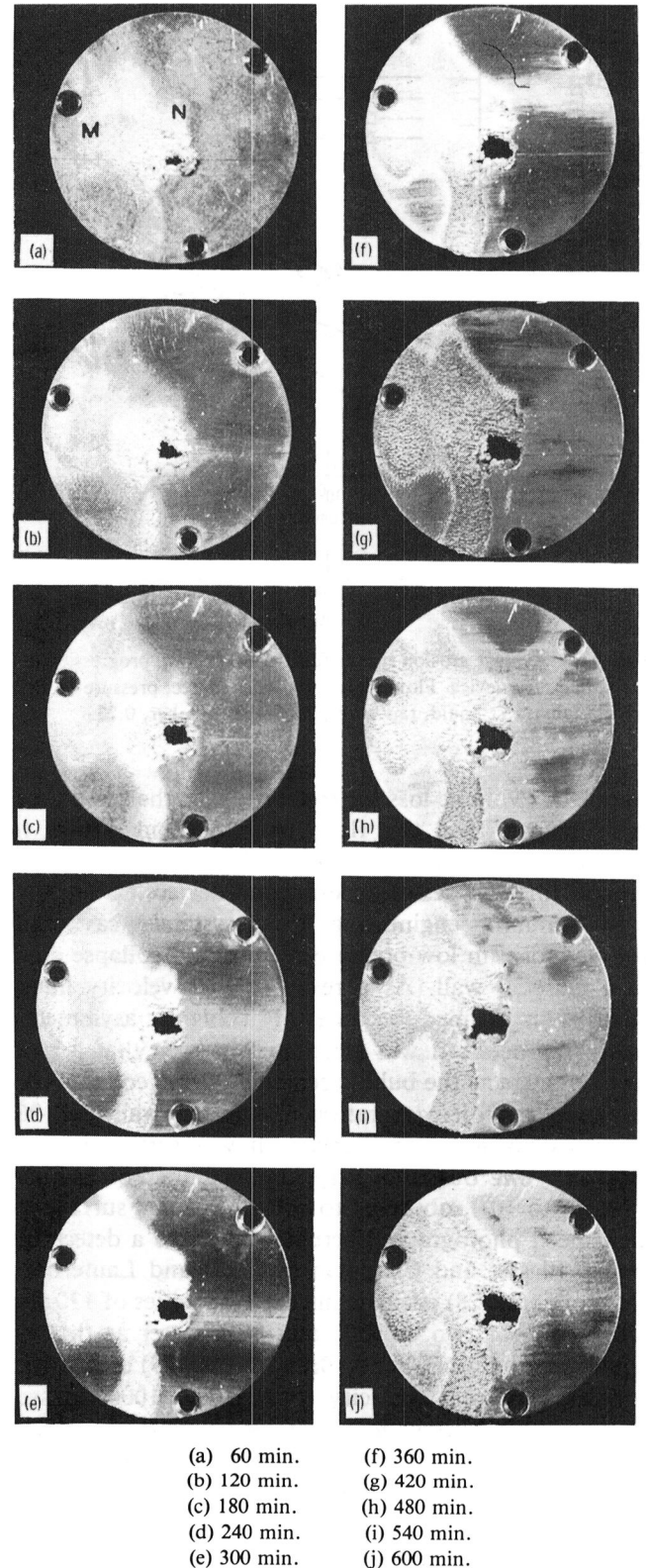


Figure 8. — Progression of erosion with time on an aluminum specimen examined in a rotating disk device (ref. 24). Flow velocity, V , 37.3 m/sec; pressure, p , 0.15 MPa (abs); diameter of the specimen, 63.5 mm; cavitation number, 0.21.

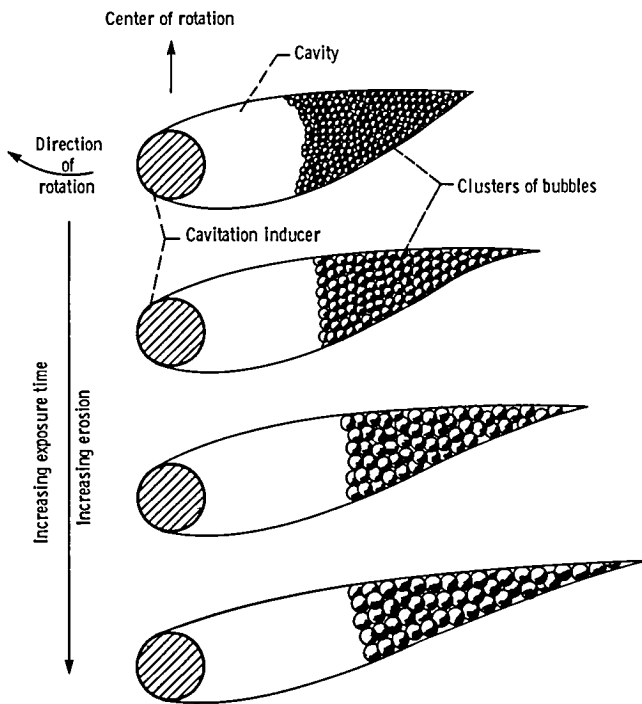


Figure 9. – Schematic of cavity size and bubble number as erosion progresses in a rotating disk device.

through the specimen thickness, etc. Deviations are also expected because of two different types of erosion versus time curves (shown schematically in figs. 10(a) and 11(a)). The erosion rate versus time curves in figures 10(b) and 11(b) show two different trends. Results further indicate the possible influences of the threshold conditions in parametric studies, the scale effects, etc., during the experimental observations.

Unified Relationship for Different Materials Tested in Other Laboratories and Devices

To check the universal nature of the average erosion rate versus erosion curves and to confirm the results of the present investigation, typical sets of erosion data using venturi (refs. 31), magnetostriction (refs. 36 to 39), and liquid impingement (refs. 40 to 42) devices were analyzed, and the results are presented in figures 12 to 19. The details of venturi, magnetostriction, and liquid impingement devices and their descriptions are presented in the appendix. The correlation coefficients, exponents, and coefficients for the power-law relation as well as the parameters for the instantaneous erosion rate versus time curves and the average erosion rate versus time curves are presented in table II for venturi data, in table III for

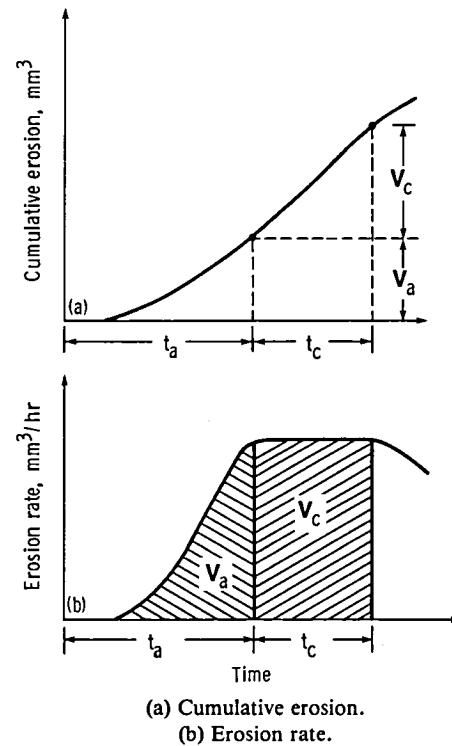


Figure 10. – Typical type I erosion-time curves.

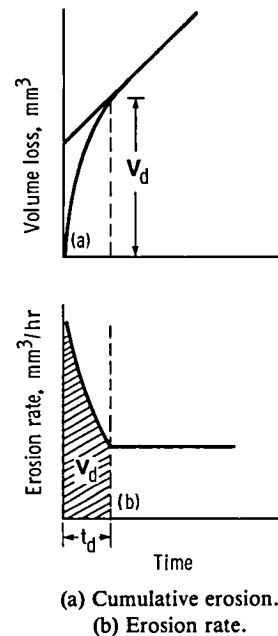


Figure 11. – Typical type II erosion-time curves.

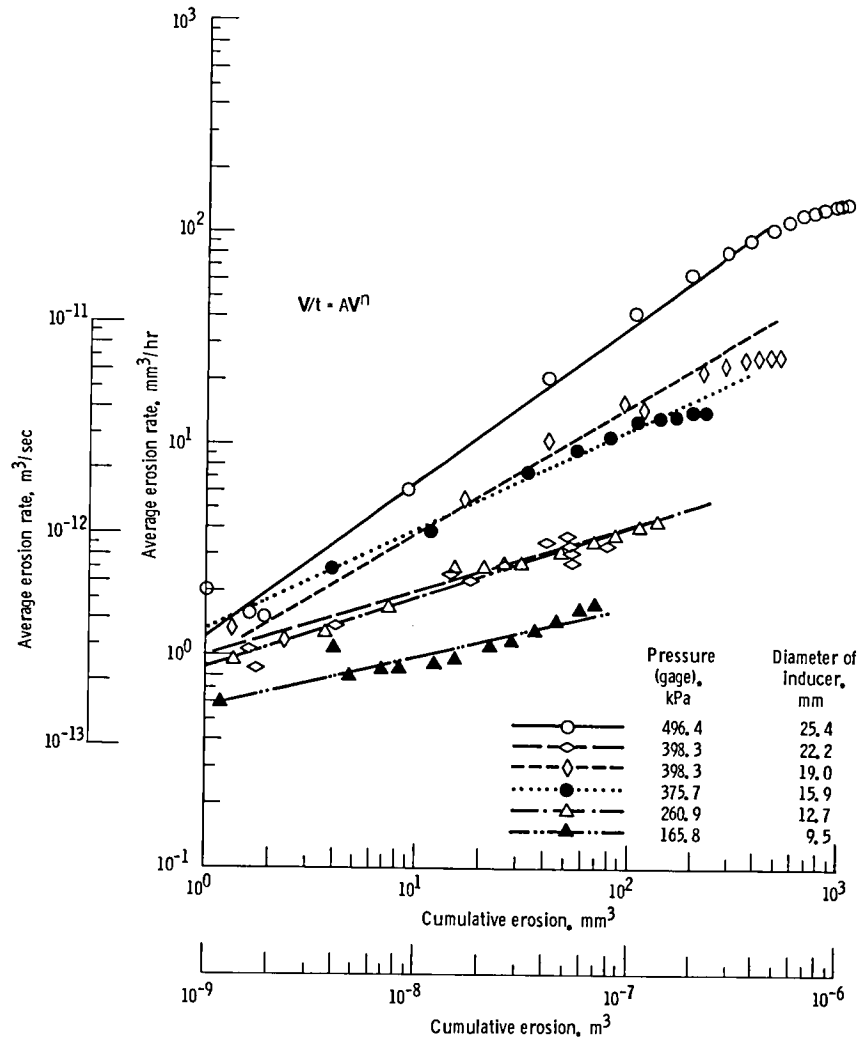


Figure 12. – Average erosion rate as function of erosion progression in a venturi device. Flow velocity, V , 27.45 m/sec. (Data source, ref. 31.)

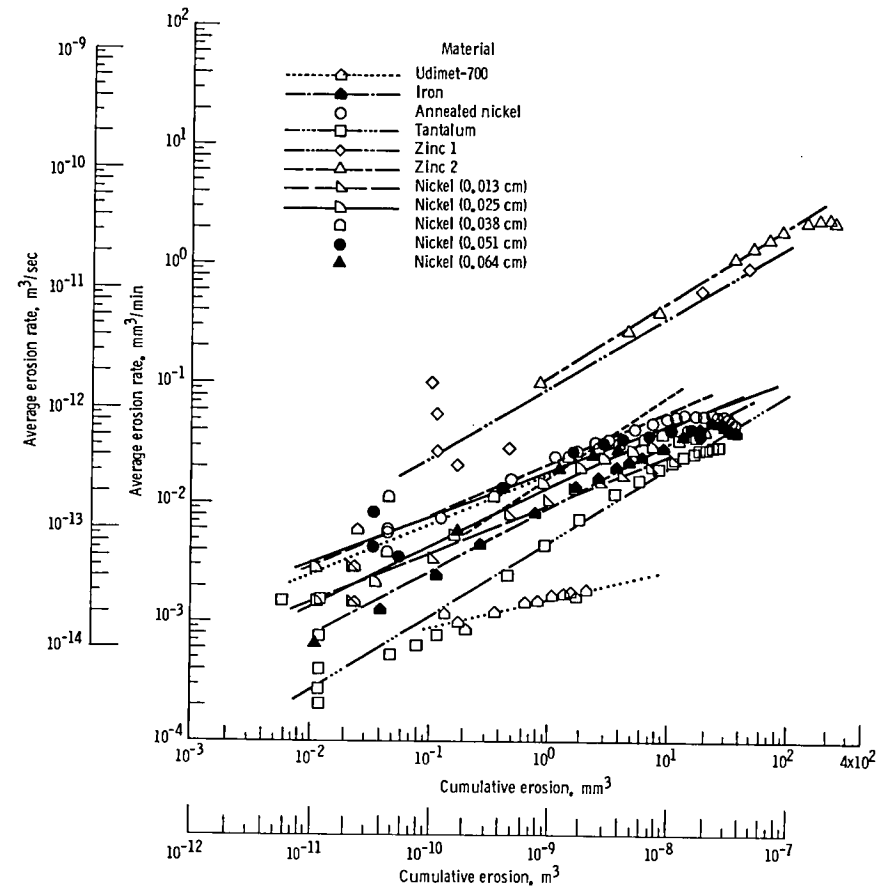


Figure 13. – Average erosion rate as function of erosion progression in a magnetostriction apparatus using both stationary and vibrating specimens. Frequency, 25 kHz; amplitude, 44.5 μm ; test liquid, water. (Data source, refs. 36 and 37.)

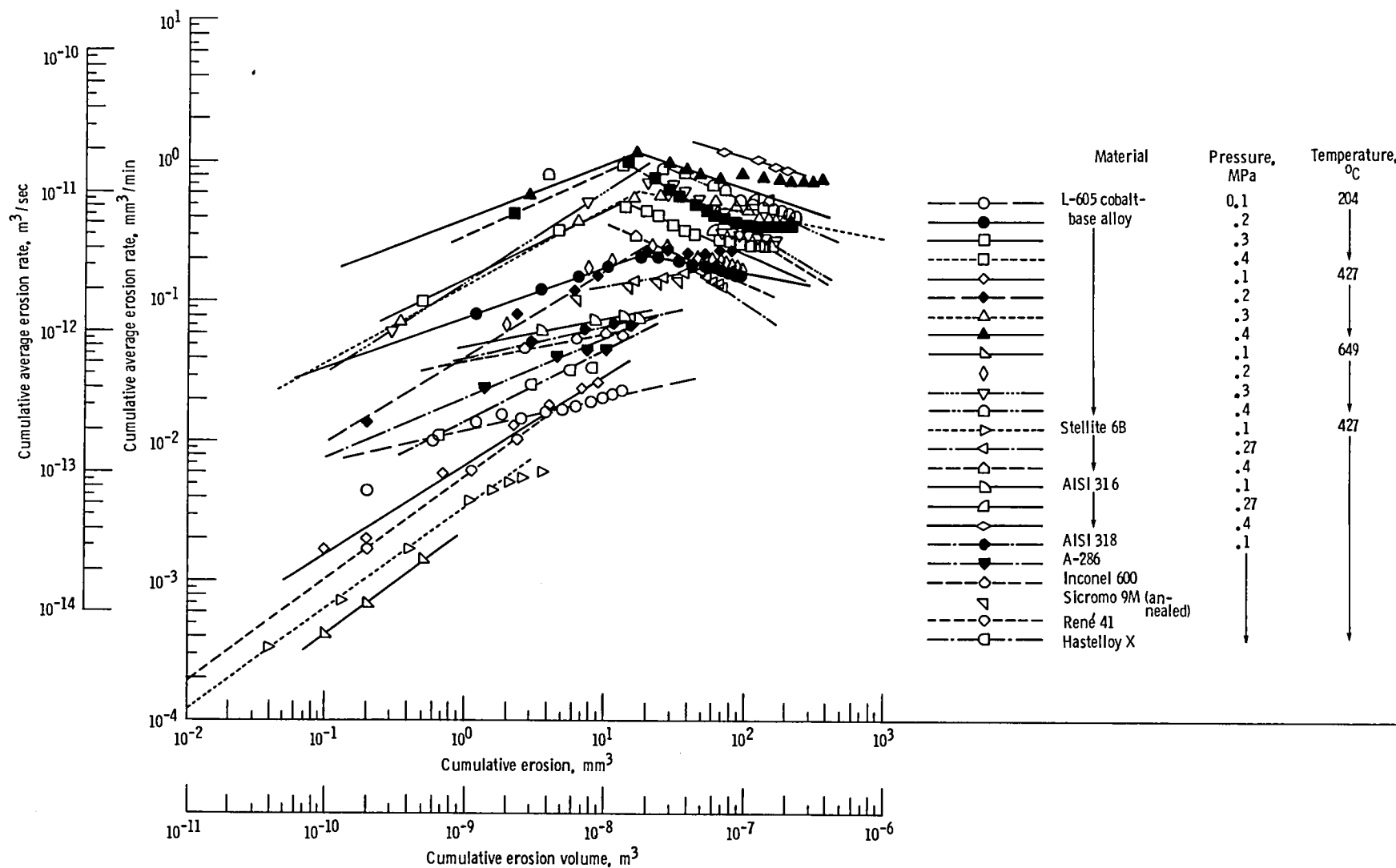


Figure 14. — Cumulative erosion rate as function of erosion progression in a magnetostriction apparatus using vibrating specimens. Frequency, 25 kHz; amplitude, 44.5 μm ; test liquid, liquid sodium. (Data source, refs. 38 and 39.)

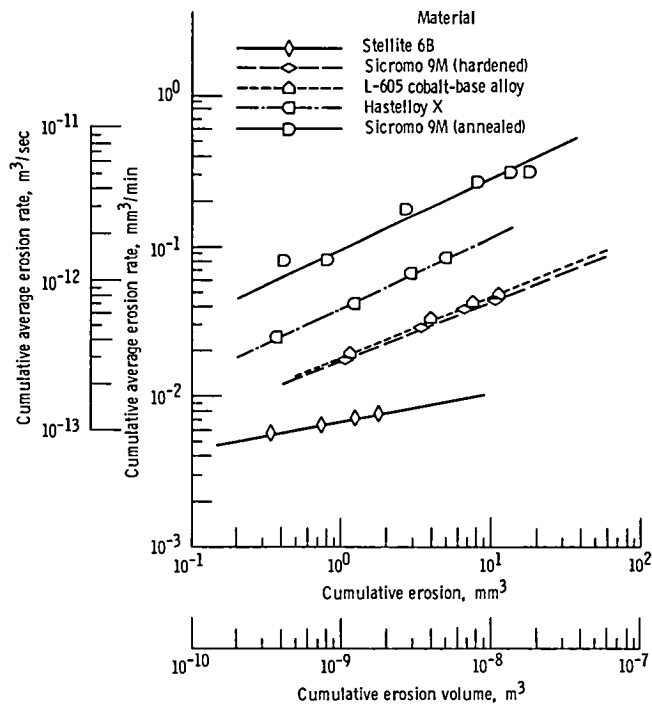


Figure 15. – Cumulative erosion rate as function of erosion progression in a magnetostriction apparatus using vibrating specimens. Frequency, 25 kHz; amplitude, 44.5 μm ; pressure, 0.1 MPa; test liquid, mercury; temperature, 149° C. (Data source, ref. 38.)

magnetostriction oscillator data, and in table IV for liquid impact data. These tables show that the exponents n and coefficients A in equation (1) vary widely for different materials and experimental conditions. The values of the exponents n and m are approximately equal ($n \approx m$) in a magnetostriction apparatus in most cases. On the other hand, for liquid impingement devices most m values for stellite and copper are more than unity. It is necessary to remember that physical limitations of the area of erosion in magnetostriction and liquid impingement devices limit the power-law relationship. Hence, further studies are necessary to understand the relationships between n and m values for a wide spectrum of materials using different type of experimental devices.

It is clear from figures 12 to 19 that each material is represented by a power-law during the acceleration zone and that the experimental points agree well with the least-squares-fit lines drawn. In addition, the empirical relations further support the view that the predominate operative phenomena appear to be the same in all types of erosion.

Figure 20 presents a typical set of macrographs of the erosion progression with respect to time for an iron specimen examined in a magnetostriction oscillator (ref. 36) during the acceleration zone. Unlike the specimens tested in a rotating disk device, the photographs in figure 20 show an increase in the area of erosion (up to 45 min) and then an increase in the depth of erosion (up to 840

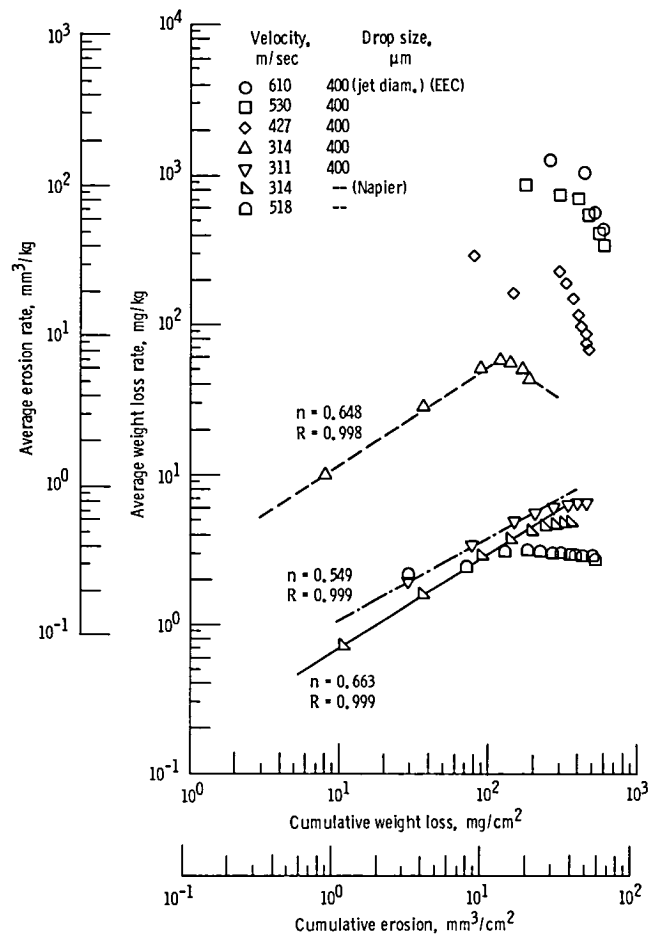


Figure 16. – Cumulative erosion rate as function of erosion progression in three liquid impact devices. (Data source, ref. 40.)

min, which resembles a honeycomb structure). In light of the limited area of the specimen, the erosion and bubble dynamics may vary with respect to time, but the general dynamics appear to be the same. During the acceleration zone the bubble cloud appeared to increase with time. Suezawa, et al. (ref. 43), noted that during the acceleration period new pits are initiated and pit density increases to a maximum.

Most of the data presented in figures 12 to 19 represent the acceleration zone since the experiments were not conducted for long exposures. In most cases the data for the deceleration zones were not available. Despite this, the deceleration zones in magnetostriction devices are due mainly to the complex interaction of the effect of changing surface geometry on the fluid dynamics of the cavitation field and the gas trapped in the large cavities.

While reporting erosion rate versus time curves, Plesset and Devine (ref. 2) observed a considerable reduction in the cavitation cloud as a consequence of hydrodynamic damping effects over the deeply damage surface area. On the other hand, Suezawa, et al. (ref. 43), stated that while the number of pits remain constant they widen and

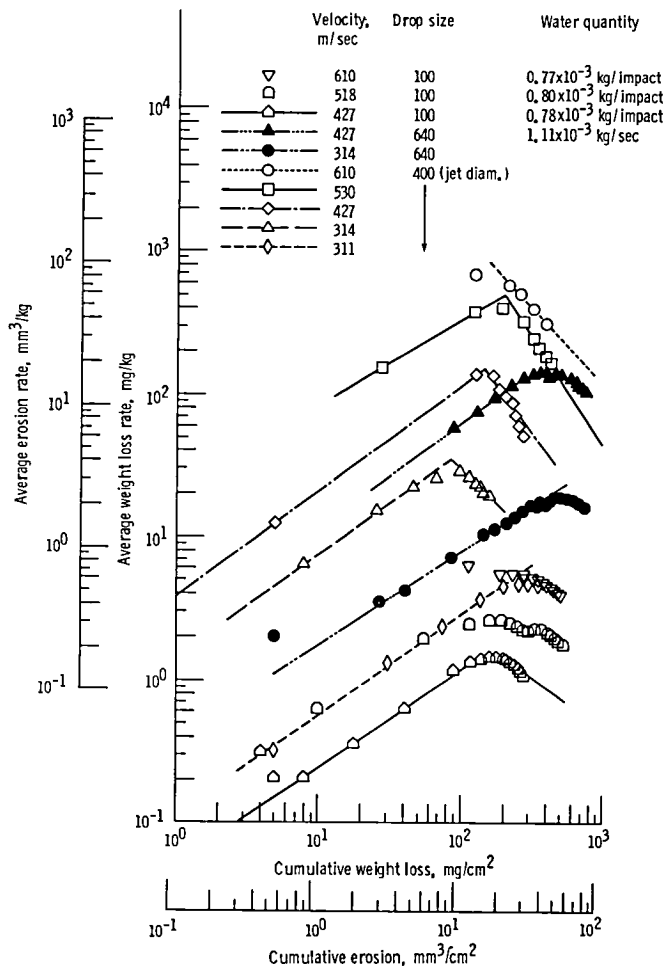


Figure 17. — Cumulative erosion rate as function of erosion progression of Stellite 6B tested in three liquid impact devices. (Data source, ref. 40.)

deepen and thus reduce the erosion in the deceleration zone. Tichler and de Gee (ref. 4) also postulated that bubbles trapped in the deep craters cause a cushioning effect and result in attenuation or a deceleration period. Similar observations were reported and similar conclusions were arrived at by others (refs. 44 to 46). Hobbs (ref. 20) stated that the decrease in the erosion rate was definitely associated with the appearance of a honeycomb-type texture on the eroded specimens. Under the same experimental conditions, Hammitt (discussion in ref. 20) observed that the rate began to decrease because of surface roughening (characterized by deep pits).

From the foregoing the magnitude of erosion in a field system can be predicted using the data from a laboratory device. However, the laboratory conditions must be fixed as close as possible to the field conditions to obtain the coefficient and exponent values of equation (1). It is, however, possible to construct deceleration curves from V_{peak} and the relations of n and m as explained in a subsequent section.

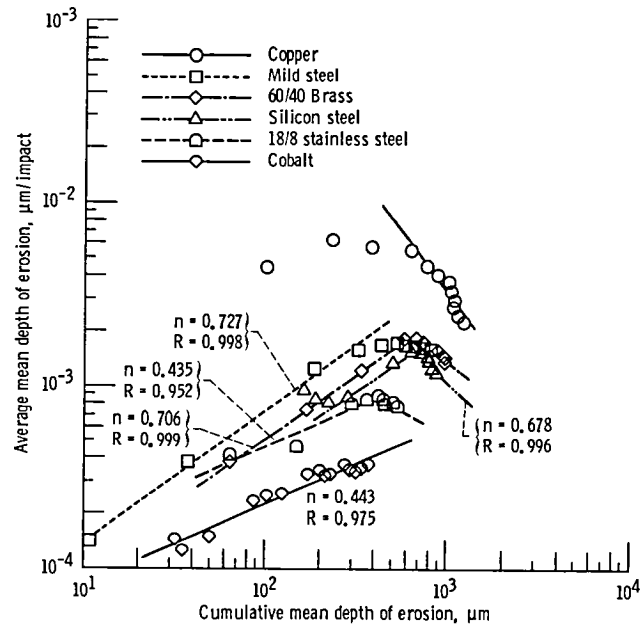


Figure 18. — Cumulative erosion rate as function of erosion progression in a drop impingement device. Velocity of drop, 125 m/sec; diameter of drop, 1.5 mm. (Data source, ref. 41.)

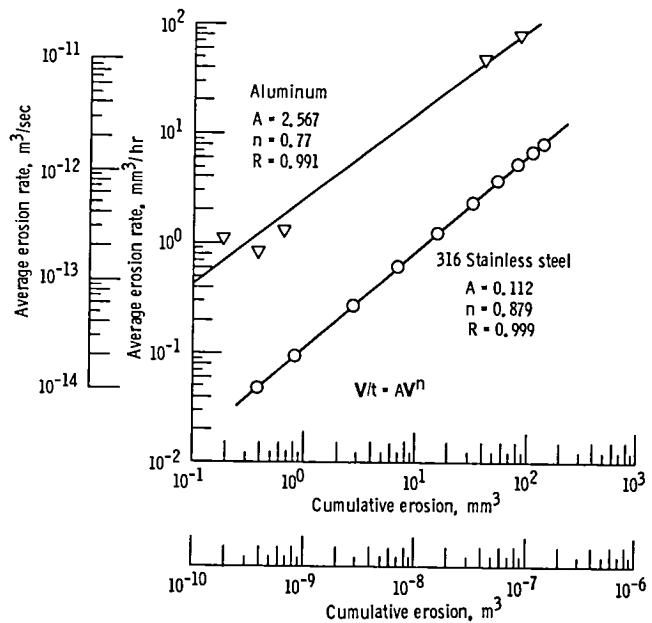


Figure 19. — Average erosion rate as function of erosion progression in liquid impingement device. Velocity of jet, 14 m/sec (resultant velocity, 95 m/sec); diameter of jet, 5 mm. (Data source, ref. 42.)

Relation Between the Coefficients and Material Properties

In this section attempts are made to establish a relation between the coefficients in equation (1) and the various mechanical properties of materials such as hardness, tensile strength, yield strength, elastic modulus, etc. Preliminary results indicate that correlations such as

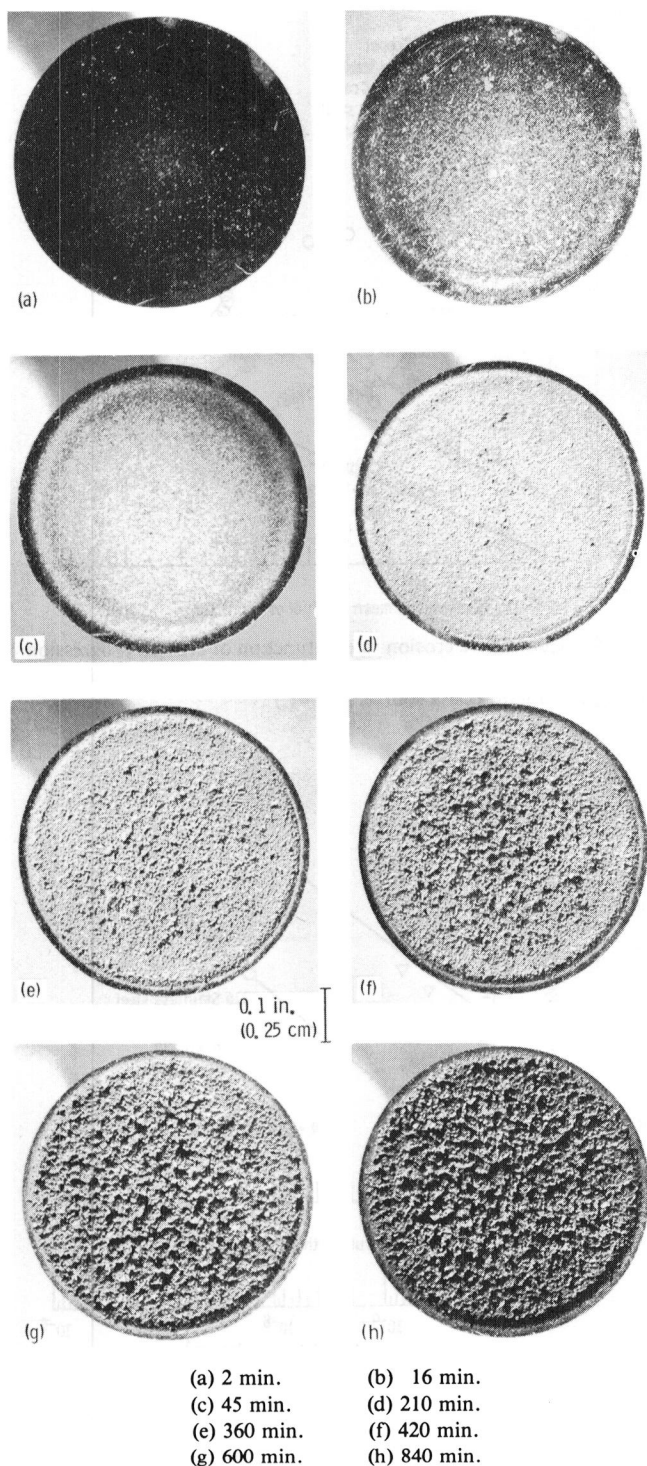


Figure 20.—Progression of erosion with time on an iron specimen examined in a magnetostriction apparatus. Frequency, 25 kHz; amplitude, 44.5 μ m; specimen diameter, 15.87 mm; distance between stationary specimen and horn, 2.5 mm; test liquid, water; temperature, 24° C (ref. 36).

these are good as long as other parameters are kept constant while examining material properties. However, if the individual parameters such as velocity, inducer diameter, pressure, etc., are changed but the same material is used, the individual correlations are close to ordinary parametric studies as shown in the next section.

Parametric Studies

In light of the observations in the previous section, it is possible to study the effect of various parameters on erosion using the coefficients obtained. Parametric studies were conducted using the following relationships:

$$\text{Erosion rate} \propto Vp^1$$

$$\text{Average erosion rate (peak)} \propto Vp^2$$

$$A \propto Vp^3$$

The results in table V clearly indicate not only a successful parametric study but also a method to assess coefficients as a function of particular parameter such as velocity. Hence, this study appears to provide tools for calculating the coefficients necessary to predict erosion in the acceleration zone and for long-term operations.

Construction of V/t Versus V Curves with n or m and Some Data Points

In most real situations, both in experiments and in erosion in field devices, results may not be obtained in precise equal time intervals. Hence, it is highly probable that the experimental data points obtained may not be complete enough to give an accurate value of the erosion rate, especially for long-term operation. A typical set of plots of available data for aluminum examined in a rotating disk device at different pressure conditions and at a constant flow velocity of 37.3 m/sec (ref. 24) is presented in figure 21. In all the curves, the acceleration zones are missing as the experimental data points collected were for large time intervals.

To demonstrate the technique of using equations (1) and (4), the acceleration zone is reconstructed using (1) the relation $m \approx n$ (since the experimental results are from a rotating disk device) and (2) the approximate experimental peak cumulative erosion V_{peak} . With a knowledge of V_{peak} and coefficient B , the values of (1) the time t_{peak} corresponding to V_{peak} and (2) the coefficient A may be calculated using the relations

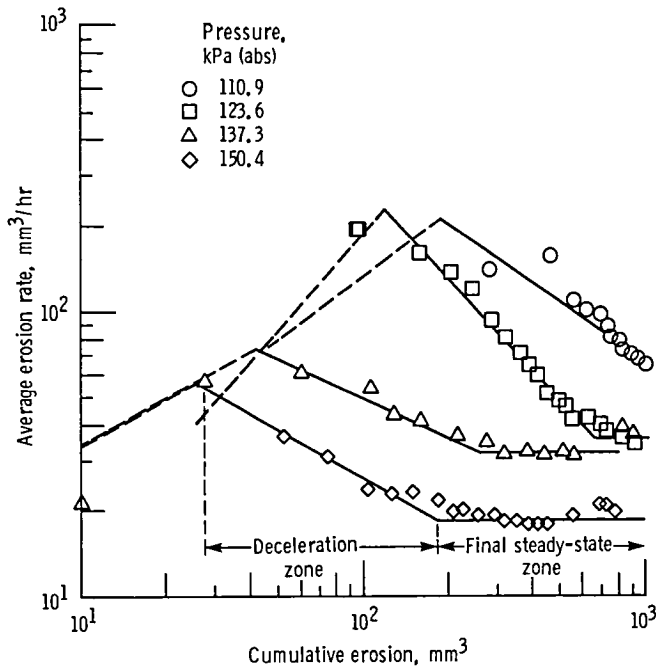


Figure 21. — Average erosion rate as function of erosion progression of aluminum tested in rotating disk device at different pressure conditions. Construction of the acceleration zones. Velocity, 37.3 m/sec.

$$V_{\text{peak}} = (B/A)^{1/(n+m)} \approx (B/A)^{1/2} m$$

and

$$V_{\text{peak}} = (Bt_{\text{peak}})^{1/(1+m)}$$

This method is limited to conditions where $n \approx m$. It was observed especially for liquid impingement devices where the values of m were more than unity, as high as 1.54 (see table IV). Hence, a modified method is to be adopted for these experimental devices after a further thorough study of the relationships between n and m and their influences on the physical and mechanical properties of materials and fluid parameters.

Prolonged Operations

The curves in figure 21 also show that as exposure to erosion increases the average erosion rates decrease further after the deceleration zone and appear to become independent of cumulative erosion (or exposure time). This phenomenon may be clear from the curves for the following conditions: 0.15 MPa pressure following 200 mm³ volume loss; 0.14 MPa following 300 mm³; 0.12 MPa following 1000 mm³; and 0.11 MPa following 1200 mm³. This indicates that as pressure increases (or intensity of erosion decreases) the cumulative erosion to attain the final steady-state zone decreases. A transition region also appears between the deceleration zone and the so-called final steady-state zone. This is similar to curves presented by Tichler and de Gee (ref. 4) and Elliott, et al. (ref. 40), who stated that there are two steady-state regions.

Summary of Results

The following summarize the results of this study:

1. The empirical power-law relationship proposed between average erosion rate and erosion volume was also used to describe the acceleration and deceleration zones of erosion. This empirical power-law relationship has been adequately demonstrated for a rotating disk device.

2. A power-law relationship is also observed during the acceleration zone for the extensive erosion data from venturi, magnetostriction, and liquid impingement devices.

3. The advantages of this power-law relationship are (1) to unify the data for various materials and cavitation erosion processes (produced by rotating disk, venturi, magnetostriction, etc.) and possibly to predict erosion rates for long-time operations, and (2) to construct curves where there are missing experimental data points.

Lewis Research Center
National Aeronautics and Space Administration
Cleveland, Ohio

Appendix—Description of Experimental Devices Used in Other Laboratories

Venturi Device

The venturi device or two-dimensional open-circuit water tunnel (fig. 22, top) consists of a 152-mm-diameter pipeline with a pressure regulating chamber, a bypass needle valve, contracting cone, test section, and diffuser. The contraction cone was used to transform a 152-mm-diameter circular section to a 101.6-mm-high and 12.7-mm-wide rectangular section. The details of the test section including the position of the test specimens and the cavitation inducer are shown in figure 22 (bottom). The test specimens are mounted on either wall with the 12.7-mm-thick cavitation inducers having 9.5- to 25.4-mm diameters extending fully over the width of the test section. The experimental conditions are: flow velocity, 27.45 m/sec, and pressure, 0.17 to 0.5 MPa (gage).

Magnetostriction Apparatus

Vibrating Specimen

The apparatus used with a vibrating specimen is shown schematically in figure 23(a). Figure 23(a) illustrates the vacuum dry-box arrangement, magnetostrictive transducer assembly, and separately sealed liquid-metal test chamber with associated argon line, vapor trap, and pressure gage. The dry box and test chamber were evacuated to a pressure of approximately 0.13 N/m^3 (10^{-3} torr) and backfilled with high-purity argon prior to testing.

The specimen was attached to the end of a resonant system consisting of a transducer, an exponential horn, and an extension-rod specimen holder. The amplitude and frequency of vibration were detected by a magnetic pickup and read on an oscilloscope. An automatic feedback system was maintained at a constant amplitude irrespective of variations in resonant frequency induced by temperature changes.

When the transducer assembly was lowered into position, a sleeve attached to the nodal flange on the amplifying horn sealed the liquid-metal test chamber from the dry box, and the test chamber pressure was regulated through a separate argon line. Pressures were measured with a precision pressure gage having an accuracy of 0.25 percent.

Stationary Specimen

A schematic diagram of the apparatus used with a stationary specimen is shown in figure 23(b), and a more

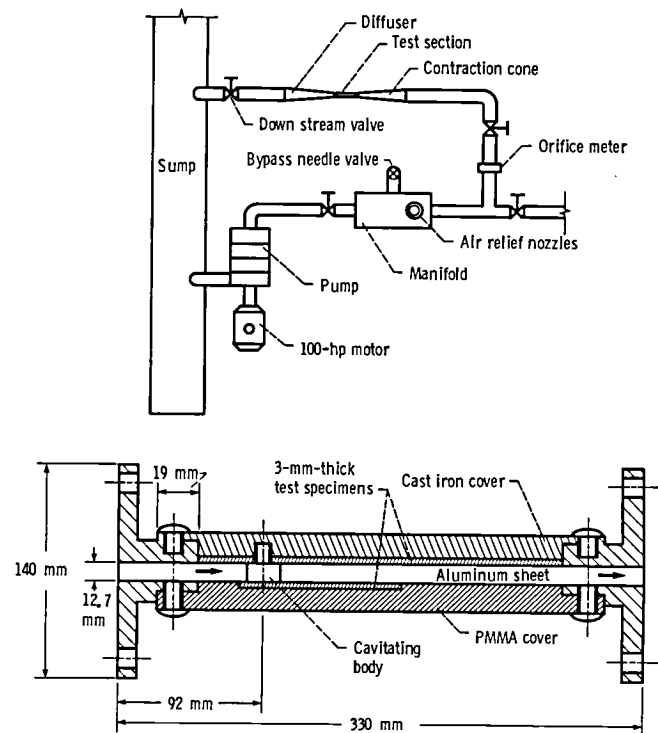
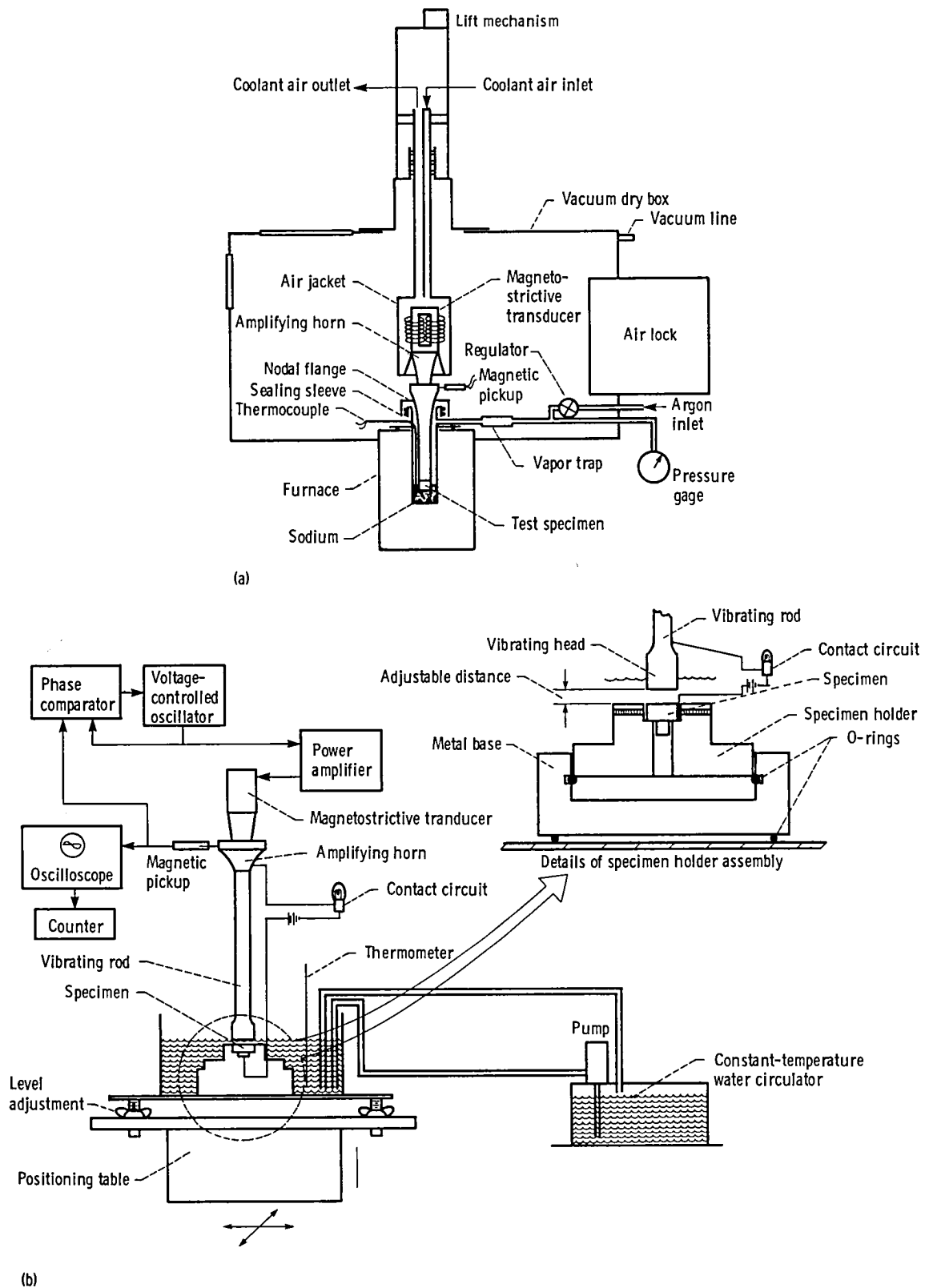


Figure 22. — Layout of two-dimensional water tunnel (top) and sectional plan of water tunnel test section (bottom) (ref. 24).

detailed schematic diagram of the specimens and holder assembly is shown in the insert. A magnetostrictive transducer was used to vibrate a rod with its free end immersed in distilled water. This end of the vibrating rod, called the vibrating head, was detachable and was made from L-605, a moderately cavitation-damage-resistant material. The head was replaced three times during the entire program, although very little damage was noted to the L-605. The test specimen, shown in the figure, was mounted directly below the vibrating head. Cavitation bubbles induced in the water by vibration collapsed on the face of the stationary specimen where they caused damage.

Magnetic pickup was used to monitor the vibration amplitude (fig. 23(b)). A feedback signal ($\sim 25 \text{ kHz}$) from the magnetic pickup kept the transducer input frequency matched to the natural resonant frequency of the transducer assembly. Level and translational adjustments and a contact circuit were used to position vibrating head and specimen surfaces and to obtain parallel measured gaps between the specimen and the vibrating head. Water temperatures were held constant by a water circulator capable of either heating or cooling the distilled water test fluid.



(a) Vibrating test specimen.
 (b) Stationary test specimen.
 Figure 23. — Schematic diagram of magnetostriction cavitation apparatus (ref. 19).

Description of Liquid Impact Devices

English Electric Company Device

The English Electric Company (EEC) device has four specimen holders equally spaced on a 457-mm- (18-in.-) diameter disk which is rotated in a vacuum chamber. A cylindrical jet of water is directed from a stationary glass nozzle of 0.39-mm (0.0153-in.) bore at right angles to the plane of the disk. Stroboscopic viewing of the jet in the test rig under normal running conditions showed that it is continuous and does not break into droplets; thus, a length equal to the width of the specimen face (8.3 mm (0.325 in.)) is cut from the jet by each specimen during a single revolution. Tests were confined to rectangular specimens—8.33 mm (0.325 in.) wide normal to the direction of rotation, 6.25 mm (0.25 in.) high, and 1.96 mm (0.077 in.) thick.

C. A. Parsons' Device

The C. A. Parsons' (CAP) erosion device has two separately driven contrarotating mild steel disks with four specimens mounted at the perimeter of the larger disk and two water sprayers on the other. Impact speeds of up to 610 m/sec (2000 ft/sec) can be obtained with comparatively low stresses. Both jets and specimens are enclosed in a vacuum chamber. The flow rate to both nozzles is 1.14×10^{-4} m³/sec (1.5 gal/min), which corresponds to theoretical water quantities of 0.736 mg/impact at 505 m/sec (1000 ft/sec), 0.781 mg/impact at 427 m/sec (1400 ft/sec), 0.800 mg/impact at 518 m/sec (1700 ft/sec), and 0.771 mg/impact at 610 m/sec (2000 ft/sec). To achieve the 610 m/sec (2000 ft/sec) impact condition, the sprayer shaft speed had to be raised from 10 000 to 12 000 rpm, which reduced the water quantity per impact. For the other impact velocities the sprayer shaft speed was held constant at 10 000 rpm, the variation in water quantity being due to the specimens being progressively tilted to achieve normal impact. The specimens, 12.7 mm (1/2 in.) in diameter and 3 mm (1/8 in.) thick, are orientated to give normal impact with the water droplets.

Napier Device (CEGB Marchwood)

The Napier device has two 1.26-m- (4-ft-) diameter disks rotating in separate vacuum chambers. Water is injected radially inward toward the rim of the disk at the horizontal centerline through a nozzle block which contains a row of small (330- μ m-diam) holes (fig. 24). The natural breakup of the jets produces a curtain of water droplets of 640- μ m Sauter mean diameter ($SMD = \Sigma d^3 / \Sigma d^2$) and of intensity 4.6 mg/cm² at one position in the path of the specimens. Two specimens, 18.7-mm (0.735 in.) in diameter and 6.4 mm (0.25 in.)

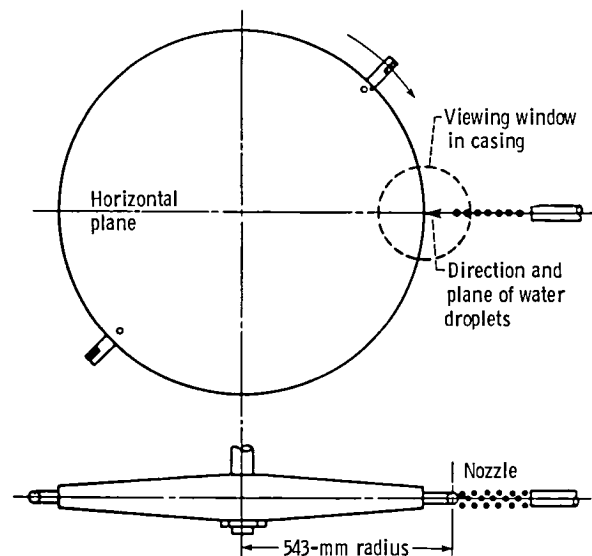


Figure 24. – Napier erosion test device (ref. 40).

thick, are mounted in holders on the rim of the disks and are positioned to give normal impact at a velocity of 311 m/sec (1020 ft/sec).

High-Speed Erosion Machine (CEGB)

The high-speed erosion machine (HSEM) at Marchwood (fig. 25) has a 599-mm (22-in.) horizontal arm rotating in a vacuum chamber and carrying a 6.3-mm (1/4-in.) square test specimen at each end. A spray block assembly similar to that used in the Napier

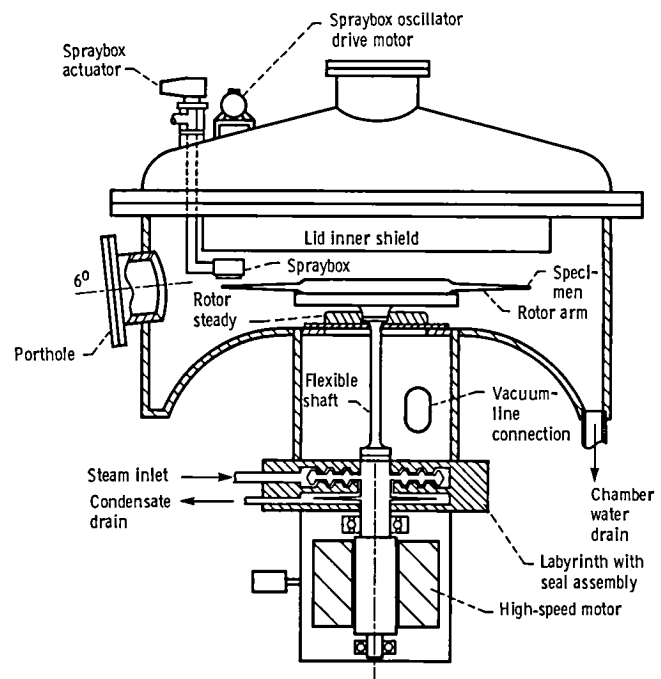


Figure 25. – High-speed erosion test machine (HSEM) (ref. 40).

machine is mounted above the rotor and is oscillated to provide a spread of droplets across 19.1 mm (3/4 in.) of the specimen face. For the supplementary droplet size program two further nozzle blocks were manufactured with the drillings reduced from 330 to 178 and 102 μm to give droplet sizes of 640, 330, and 290 μm (SMD). Consequently, the quantity of water per impact was reduced from 4.27 to 1.26 and 0.41 mg/cm^2 .

References

1. Thiruvengadam, A.; and Preiser, H. S.: On Testing Materials for Cavitation Damage Resistance. *Journal of Ship Research*, vol. 8, no. 3, Dec. 1964, pp. 39-56.
2. Plesset, M. S.; and Devine, R. E.: Effect of Exposure Time on Cavitation Damage. *J. Basic Eng.*, vol. 88, no. 4, Dec. 1966, pp. 691-705.
3. Heymann, F. J.: On the Time Dependence of the Rate of Erosion Due to Impingement or Cavitation. *Am. Soc. Test. Mater. Spec. Tech. Publ.* (408), 1967, pp. 70-110.
4. Tichler, J. W.; and de Gee, A. W. J.: Time Dependence of Cavitation Erosion and Effect of Some Material Properties. *Proceedings of the Third International Conference on Rain Erosion and Associate Phenomena*. Vol. II, A. A. Fyall and R. B. King, eds., Royal Aircraft Establishment, (London), 1970, pp. 847-879.
5. Hammitt, F. G.: Cavitation Erosion: The State of the Art and Predicting Capability. *Appl. Mech. Rev.*, vol. 32, no. 6, June 1979, pp. 665-675.
6. Hammitt, F. G.: *Cavitation and Multiphase Flow*. McGraw-Hill Book Co., 1980.
7. Rao, P. V.; Rao, B. C. S.; and Rao, N. S. L.: Correlating Models and Prediction of Erosion Resistance to Cavitation and Drop Impact. *J. Test. Eval.*, vol. 4, no. 1, Jan. 1976, pp. 3-14.
8. Engel, O. G.: A First Approach to a Microscopic Model of Erosion Rate in Drop Impact and Cavitation. *Proceedings of the Third International Conference on Rain Erosion and Associate Phenomena*. Vol. I, A. A. Fyall and R. B. King, eds., Royal Aircraft Establishment, (London), 1970, pp. 447-518.
9. Perelman, R. G.; and Denisov, Y. D.: Strength of Materials Under the Action of Droplet Impacts. *RAE-LIB-TRANS-1654*, Royal Aircraft Establishment.
10. Springer, G. S.: *Erosion by Liquid Impact*. Scripta Pub. Co., 1976.
11. Schmitt, G. F., Jr.: Liquid and Solid Particle Impact Erosion. *Wear Control Handbook*, M. B. Peterson and W. O. Winer, eds., American Society of Mechanical Engineers, 1981, pp. 231-282.
12. Thiruvengadam, A.: *Handbook of Cavitation Damage*. TR-233-8, Hydronautics, Inc., 1965 (AD-473532).
13. Thiruvengadam, A.: Theory of Erosion. *Proceedings of the Second Meersburg Conference on Rain Erosion and Allied Phenomena*. Vol. II, A. A. Fyall and R. B. King, eds., Royal Aircraft Establishment, (Farnborough), 1967, pp. 605-653.
14. Thiruvengadam, A.: *Handbook of Cavitation Erosion*. TR-7301-1, Hydronautics, Inc., 1974.
15. Noskievic, J.: Dynamics of the Cavitation Damage. *Proceedings of the Joint IAHR-ASME-ASCE Symposium on Design and Operation of Fluid Machinery*. Vol. II, Colorado State University, 1978, pp. 453-462.
16. Lichtarowicz, A.: Cavitating Jet Apparatus for Cavitation Erosion Testing. *Am. Soc. Test. Mater. Spec. Tech. Publ.* (664), 1979, pp. 530-549.
17. Heymann, F. J.: Toward Quantitative Prediction of Liquid Impact Erosion. *Am. Soc. Test. Mater. Spec. Tech. Publ.* (474), 1970, pp. 212-248.
18. Hoff, G.; and Langbein, G.: Resistance of Materials Towards Various Types of Mechanical Stress. *Proceedings of the Second Meersburg Conference on Rain Erosion and Allied Phenomena*. Vol. II, A. A. Fyall and R. B. King, eds., Royal Aircraft Establishment, (Farnborough), 1967, pp. 655-681.
19. Rao, P. V.; and Young, S. G.: Universal Approach to Analysis of Cavitation and Liquid-Impingement Erosion Data. *NASA TP-2061*, 1982.
20. Hobbs, J. M.: Experience With a 20-kc Cavitation Erosion Test. *Am. Soc. Test. Mater. Spec. Tech. Publ.* 408, 1967, pp. 159-185.
21. Stinebring, D. R.; Holl, J. W.; and Arndt, R. E. A.: Two Aspects of Cavitation Damage in the Incubation Zone: Scaling by Energy Considerations and Leading Edge Damage. *J. Fluids Eng.*, vol. 102, no. 4, Dec. 1980, pp. 481-485.
22. Kato, H.: A Consideration on Scaling Laws of Cavitation Erosion. *International Shipbuilding Progress*, vol. 22, no. 253, Sept. 1975, pp. 305-327.
23. Rao, P. V.; and Rao, B. C. S.: Some Erosion Studies and Scale Effects With Rotating Disk Device. *Cavitation Erosion in Fluid Systems*, W. L. Swift and R. E. A. Arndt, eds., American Society of Mechanical Engineers, New York, 1981, pp. 119-131.
24. Rao, P. V.: Characteristics, Correlations, Similarities and Prediction of Erosion due to Cavitation and Liquid Impingement. *Ph.D. Thesis*, Indian Institute of Science, Bangalore, India, 1975.
25. Gibson, D. C.: The Kinetic and Thermal Expansion of Vapor Bubbles. *J. Basic Eng.*, vol. 94, no. 1, Mar. 1972, pp. 89-96.
26. Kling, C. L.: A High Speed Photographic Study of Cavitation Bubble Collapse. *Ph. D. Thesis*, Univer. of Michigan, 1970.
27. Plesset, M. S.; and Chapman, R. B.: Collapse of an Initially Spherical Vapour Cavity in Neighbourhood of a Solid Boundary. *J. Fluid Mech.*, vol. 47, pt. 2, May 1971, pp. 283-290.
28. Lauterborn, W.; and Bolle, H.: Experimental Investigations of Cavitation-Bubble Collapse in the Neighbourhood of a Solid Boundary. *J. Fluid Mech.*, vol. 72, pt. 2, Nov. 25, 1975, pp. 391-399.
29. Brunton, J. H.: Cavitation Damage. *Proceedings of the Third International Conference on Rain Erosion and Allied Phenomena*. Vol. II, A. A. Fyall and R. B. King, eds., Royal Aircraft Establishment, (London), 1970, pp. 821-846.
30. Kling, C. L.; and Hammitt, F. G.: A Photographic Study of Spark-Induced Cavitation Bubble Collapse. *J. Basic Eng.*, vol. 94, no. 4, Dec. 1972, pp. 825-833.
31. Chandrasekhara, D. V.: Studies on Characteristics of Cavity and Cavitation Damage Behind Circular Cylinders in Water With a Venturi. *Ph.D. Thesis*, Indian Institute of Science, Bangalore, India, 1973.
32. Hammitt, F. G.: Observations on Cavitation Damage in a Flowing System. *J. Basic Eng.*, vol. 85, no. 3, Sept. 1963, p. 347-359.
33. Ivany, R. D.; Hammitt, F. G.; and Mitchell, T. M.: Cavitation Bubble Collapse Observations in a Venturi. *J. Basic Eng.*, vol. 88, no. 3, Sept. 1966, p. 649-657.
34. Robinson, M. J.; and Hammitt, F. G.: Detailed Damage Characteristics in a Cavitating Venturi. *J. Basic Eng.*, vol. 89, no. 1, Mar. 1967, pp. 161-173.
35. Rao, P. V.; Rao, B. C. S.; and Rao, N. S. L.: Erosion and Cavity Characteristics in Rotating Components. *J. Test. Eval.*, vol. 8, 1980, pp. 127-142.
36. Young, S. G.: Study of Cavitation Damage to High-Purity Metals and Nickel-Base Superalloy in Water. *NASA TN D-6014*, 1970.

37. Young, S. G.: Cavitation Damage of Stainless Steel, Nickel, and Aluminum Alloy in Water for ASTM Round Robin Tests. NASA TM X-1670, 1968.
38. Young, S. G.; and Johnston, J. R.: Accelerated Cavitation Damage of Steels and Superalloys in Sodium and Mercury. Am. Soc. Test. Mater. Spec. Tech. Publ. 408, 1967, pp. 186-212.
39. Young, S. G.; and Johnston, J. R.: Effect of Temperature and Pressure on Cavitation Damage in Sodium. Am. Soc. Test. Mater. Spec. Tech. Publ. (474), 1970, pp. 67-108.
40. Elliott, D. E.; Marriott, J. B.; and Smith, A.: Comparison of Erosion Resistance of Standard Steam Turbine Blade and Shield Materials on Four Test Rigs. Am. Soc. Test. Mater. Spec. Tech. Publ. (474), 1970, pp. 127-161.
41. Thomas, G. P.; and Brunton, J. H.: Drop Impingement Erosion of Metals. Proc. R. Soc. London, ser. A, vol. 314, no. 1519, Jan. 27, 1970, pp. 549-565.
42. Hammitt, F. G.; et al.: ASTM Round-Robin Test With Vibratory Cavitation and Liquid Impact Facilities of 6061-T6511 Aluminum Alloy, 316 Stainless Steel and Commercially Pure Nickel. Mater. Res. Stand., vol. 10, no. 10, Oct. 1970, pp. 16-23 and 36-38.
43. Suezawa, Y.; et al.: Studies on Cavitation Erosion. J. Basic Eng., vol. 94, no. 3, Sept. 1972, pp. 521-532.
44. Hammitt, F. G.: Discussion on S. G. Young and J. R. Johnston. Am. Soc. Test. Mater. Spec. Tech. Publ. (474), 1970, pp. 103-107.
45. Matsumura, M.: Influence of Test Parameters in Vibratory Cavitation Erosion Tests. Am. Soc. Test. Mater. Spec. Tech. Publ. (664), 1979, pp. 434-458.
46. Hirotsu, M.: Cavitation Damage Mechanism and Its Correlation to Physical Properties of Material. Am. Soc. Test. Mater. Spec. Tech. Publ. (474), 1970, pp. 48-66.

TABLE I. - EROSION PARAMETERS OF MATERIALS EXAMINED IN ROTATING DISK DEVICE

(a) Average and instantaneous erosion rates

Material	Diameter of cavitation inducer, m	Velocity, m/sec	Average erosion rate			Instantaneous erosion rate		
			Peak, ϵ_{ma} , m^3/sec	Cumulative erosion at peak, V_{ma} , m^3	Time to attain the peak, t_{ma} , sec	Peak, ϵ_{mi} , m^3/sec	Cumulative erosion at peak, V_{mi} , m^3	Time to attain the peak, t_{mi} , sec
Copper	25.4×10^{-3}	37.3	418.00×10^{-14}	60.2×10^{-9}	1.44×10^4	721.00×10^{-14}	17.7×10^{-9}	0.63×10^4
		36.6	-----	-----	-----	-----	-----	-----
		35.8	-----	-----	-----	-----	-----	-----
		35.0	-----	-----	-----	-----	-----	-----
Brass I	25.4×10^{-3}	37.3	168.00×10^{-14}	66.7×10^{-9}	3.96×10^4	293.00×10^{-14}	12.7×10^{-9}	1.62×10^4
		36.6	16.40	12.5	7.56	37.92	11.1	7.20
		35.8	5.28	4.5	8.28	14.17	2.9	6.84
		35.0	3.61	2.9	8.28	8.33	1.0	4.32
Brass II	25.4×10^{-3}	37.3	359.00×10^{-14}	38.7×10^{-9}	1.08×10^4	628.00×10^{-14}	19.2×10^{-9}	0.63×10^4
		36.6	88.60	51.0	5.76	183.00	44.4	5.40
		35.8	17.50	8.8	5.04	40.56	5.2	4.14
		35.0	6.11	3.9	6.48	20.56	2.6	5.40
Stainless steel	25.4×10^{-3}	37.3	64.20×10^{-14}	87.7×10^{-9}	13.68×10^4	139.00×10^{-14}	18.8×10^{-9}	5.76×10^4
		36.6	35.00	89.5	25.56	81.11	80.7	24.48
		35.8	23.89	61.3	25.56	83.06	18.5	14.22
		35.0	2.17	6.5	29.70	6.39	4.0	24.48

(b) Power-law relation parameters

Material	Diameter of cavitation inducer, m	Velocity, m/sec	Power-law relation parameters								
			Acceleration zone, ^a $V/t = AV^n$					Deceleration zone, ^a $V/t = BV^{-m}$			
			A	n	Correlation coefficient	$\epsilon_{m\dot{a}}/\epsilon_{mi}$ (b)	(1 - n)	B	m	Correlation coefficient	(1 + m)
Copper	25.4×10^{-3}	37.3	1.342	0.673	0.995	0.58	0.33	197	0.60	-0.988	1.60
		36.6	.41	.425	.976	---	.57	---	---	---	---
		35.8	.17	.534	.987	---	.47	---	---	---	---
		35.0	.10	.71	.991	---	.29	---	---	---	---
Brass I	25.4×10^{-3}	37.3	0.459	0.701	0.999	0.57	0.30	1115	1.20	-0.982	2.20
		36.6	.127	.615	.999	.43	.38	---	---	---	---
		35.8	.098	.390	.911	.37	.61	---	---	---	---
		35.0	.077	.537	.987	.43	.46	---	---	---	---
Brass II	25.4×10^{-3}	37.3	1.199	0.759	0.999	0.57	0.24	507	0.86	-0.910	1.86
		36.6	.378	.549	.994	.48	.45	---	---	---	---
		35.8	.228	.442	.989	.43	.56	---	---	---	---
		35.0	.116	.496	.968	.29	.50	---	---	---	---
Stainless steel	25.4×10^{-3}	37.3	0.184	0.616	0.989	0.46	0.38	45	0.60	-0.921	1.60
		36.6	.089	.598	---	.42	.40	---	---	---	---
		35.8	.043	.78	.998	.29	.22	---	---	---	---
		35.0	.021	.738	.998	.34	.26	---	---	---	---

^aCorrelations were carried out using mm^3/hr for average erosion rate and mm^3 for cumulative erosion.

^bValues to compute this ratio obtained from table I(a).

^cThis is a typical value which exceeds unity because specimens were damaged during experimentation.

TABLE II. - EROSION PARAMETERS OF ALUMINUM AND STAINLESS STEEL EXAMINED IN VENTURI DEVICES

(a) Average and instantaneous erosion rates

Material	Pressure, MPa	Velocity, m/sec	Test liquid	Average erosion rate			Instantaneous erosion rate		
				Peak, ϵ_{ma} , m^3/sec	Cumulative erosion at peak, V_{ma} , m^3	Time to attain peak, t_{ma}	Peak, ϵ_{mi} , m^3/sec	Cumulative erosion at peak, V_{mi} , m^3	Time to attain peak t_{mi} , sec
Aluminum ^a	0.50	27.45	Water	-----	-----	-----	561.00×10^{-13}	518×10^{-9}	1.71×10^4
	.40	↓	↓	-----	-----	-----	20.30	34	3.96
	.40	↓	↓	-----	-----	-----	144.00	169	3.24
	.38	↓	↓	-----	-----	-----	55.30	124	3.51
	.26	↓	↓	-----	-----	-----	18.10	100	9.36
	.17	↓	↓	-----	-----	-----	8.46	53	12.24
	.17	↓	↓	-----	-----	-----	-----	-----	-----
Stainless steel ^b	-----	19.7	Water	$c_0.046$	$d_7.90$	62.28×10^4	$c_0.214 \times 10^{-13}$	$d_5.86 \times 10^{-9}$	58.86×10^4
	-----	19.5	Mercury	$c_2.624$	d_{656}	90	$c_8.433$	d_{367}	77.40
	-----	10.4	Mercury	$c_e 1.328$	d_{498}	135	$c_2.375$	d_{56}	18.36
	-----	-----	-----	-----	-----	-----	-----	-----	-----

(b) Power-law relation parameters

Material	Pressure, MPa	Velocity, m/sec	Test liquid	Power-law relation parameters				
				Acceleration zone, $f V/t = AV^n$				
				A	n	Correlation coefficient	$\epsilon_{ma}/\epsilon_{mi} (g)$	(1 - n)
Aluminum ^a	0.50	27.45	Water	1.218	0.736	0.998	-----	0.26
	.40	↓	↓	1.002	.303	.920	-----	.70
	.40	↓	↓	.949	.599	.990	-----	.40
	.38	↓	↓	1.319	.475	.996	-----	.53
	.26	↓	↓	.864	.331	.988	-----	.67
	.17	↓	↓	.560	.240	.927	-----	.76
	.17	↓	↓	-----	-----	-----	-----	-----
Stainless steel ^b	-----	19.7	Water	$h_0.0095$	0.74	0.997	0.21	0.26
	-----	19.5	Mercury	$h_0.0785$.522	.976	.31	.48
	-----	10.4	Mercury	$h_0.0649$.49	.949	.42	.51
	-----	-----	-----	-----	-----	-----	-----	-----

^aDifferent sizes of inducers were used.^bSame test section was used.^cUnits are $\mu in/hr$.^dUnits are μin .^eTwo peaks have been observed.^fCorrelations were carried out using mm^3/hr for average erosion rate and mm^3 for cumulative erosion.^gValues to compute this ratio obtained from table II(a).^hCorrelations were carried out using $\mu in/hr$ for average erosion rate and μin for cumulative erosion.

TABLE III. - EROSION PARAMETERS OF MATERIALS EXAMINED IN MAGNETOSTRICTION OSCILLATORS

(a) Average and instantaneous erosion rates

Material	Test liquid	Test liquid temperature, °C	Pressure, MPa	Average erosion rate			Instantaneous erosion rate		
				Peak, ϵ_{ma} , m^3/sec	Cumulative erosion at peak, V_{ma} , m^3	Time to attain peak, t_{ma} , sec	Peak, ϵ_{mi} , m^3/sec	Cumulative erosion at peak, V_{mi} , m^3	Time to attain peak, t_{mi} , sec
Nickel (b ^{0.013})	Water ↓	---	0.10 ↓	---	---	---	---	---	---
Nickel (b ^{0.025})		---		---	---	---	0.66x10 ⁻¹²	9.40x10 ⁻⁹	18.00x10 ³
Nickel (b ^{0.038})		---		---	---	---	.73	7.50	12.60
Nickel (b ^{0.051})		---		0.70x10 ⁻¹²	10.00x10 ⁻⁹	14.4x10 ³	.90	8.40	12.60
Nickel (b ^{0.064})		---		.59	8.47	14.4	.74	3.04	6.30
Udimet		---		---	---	---	---	---	---
Zinc 1		---		---	---	---	---	---	---
Zinc 2		---		39.32	177.00	4.5	64.68	75.50	2.55
Tantalum		---		---	---	---	.78	19.70	41.40
Iron		---		.81	26.10	32.0	1.44	15.60	23.40
Annealed nickel		---		.91	16.50	18.0	1.18	8.30	9.90
L-605	Sodium	204	0.10	---	---	---	---	---	---
			.20	3.43x10 ⁻¹²	18.50x10 ⁻⁹	5.4x10 ³	4.45x10 ⁻¹²	14.50x10 ⁻⁹	4.50x10 ³
			.30	7.83	14.10	1.8	10.45	9.40	1.35
	Sodium	427	0.10	---	---	---	---	---	---
			.20	3.95x10 ⁻¹²	28.40x10 ⁻⁹	7.2x10 ³	6.33x10 ⁻¹²	15.00x10 ⁻⁹	4.50x10 ³
			.30	9.33	25.20	2.7	11.88	11.05	1.35
	Sodium	649	0.10	---	---	---	---	---	---
			.20	4.02x10 ⁻¹²	21.70x10 ⁻⁹	5.4x10 ³	6.55x10 ⁻¹²	4.95x10 ⁻⁹	2.25x10 ³
			.40	11.72	21.10	1.8	15.00	14.35	1.35
Stellite 68	Sodium	427	0.10	---	---	---	0.19x10 ⁻¹²	0.75x10 ⁻⁹	16.20x10 ³
			.27	2.78x10 ⁻¹²	49.20x10 ⁻⁹	18.0x10 ³	3.33	33.00	12.60
			.40	4.75	17.10	3.6	17.10	8.55	1.81
	AISI 316 stain- less steel	---	.10	1.28	13.80	10.8	1.44	11.20	9.00
			.27	---	---	---	---	---	---
			.40	19.72	71.00	3.6	19.72	35.50	1.80
	AISI 318 A-286 Inconel 600 Sicromo 9M (annealed) Rene 41 Hastelloy X	---	.10	---	---	---	1.29	9.48	9.00
			.27	---	---	---	.92	3.10	5.40
			.40	---	---	---	1.10	8.40	9.00
Stellite 68 Sicromo 6M (hardened) L-605 Hastelloy X Sicromo 6M (annealed)	Mercury ↓	149 ↓	0.10 ↓	---	---	---	---	---	---
				---	---	---	---	---	---
				---	---	---	---	---	---
				---	---	---	---	---	---
				---	---	---	---	---	---

^aCorrelations performed using mm³/min of average erosion rate and mm³ at cumulation erosion.^bDistant in cm between the horn and stationary specimen.^cOnly two data points available.^dOnly three data points available.

TABLE III. - Concluded. EROSION PARAMETERS OF MATERIALS EXAMINED IN MAGNETOSTRICTION OSCILLATORS

(b) Power-law relation parameters

Material	Test liquid	Test liquid temperature, °C	Pressure, MPa	Power-law relation parameters								
				Acceleration zone, ^a $V/t = AV^n$					Deceleration zone, ^a $V/t = BV^{-m}$			
				A	n	R	$\epsilon_{ma}/\epsilon_{mi}$ (b)	(1 - n)	B	m	R	(1 + m)
Nickel (C0.013)	Water	---	0.10	0.0095	0.408	0.980	---	0.59	---	---	---	---
Nickel (C.025)		---		.013	.502	.996	---	.50	---	---	---	---
Nickel (C.038)		---		.018	.430	.987	---	.57	---	---	---	---
Nickel (C.051)		---		.019	.396	.954	---	.60	---	---	---	---
Nickel (C.064)		---		.017	.687	.997	---	.31	---	---	---	---
Udimet		---		.0015	.239	.922	---	.76	---	---	---	---
Zinc 1		---		.093	.60	.951	---	.40	---	---	---	---
Zinc 2		---		.111	.644	.999	---	.36	---	---	---	---
Tantalum		---		.005	.627	.986	---	.37	---	---	---	---
Iron		---		.009	.542	.996	---	.46	---	---	---	---
Annealed nickel		---		.022	.438	.997	---	.56	---	---	---	---
L-605	Sodium	204	0.10	0.0119	0.225	0.974	---	0.77	---	---	---	---
			.20	.0759	.349	.999	0.77	.65	0.359	0.180	-0.990	1.18
			.30	.1420	.509	(d)	.75	.49	1.607	.433	-.971	1.43
			.40	.2960	.450	(d)	.79	.55	4.912	.598	-.994	1.60
	Sodium	427	0.10	0.0068	0.639	0.996	---	0.36	---	---	---	---
			.20	.0395	.620	.995	0.62	.38	---	---	---	---
			.30	.129	.549	e .995	.79	.45	1.070	0.194	-0.969	1.19
			.40	.386	.383	(d)	.80	.62	2.874	.326	-.992	1.33
	Sodium	649	0.10	0.0023	0.751	e0.999	---	0.25	---	---	---	---
			.20	---	---	---	---	---	---	---	---	---
			.30	.134	.668	(d)	.78	.33	5.021	0.588	-0.981	1.59
			.40	---	---	---	---	---	4.181	.448	-.990	1.45
Stellite 68	Sodium	427	0.10	0.0033	0.719	0.999	---	0.28	---	---	---	---
			.27	.085	.176	e .993	0.83	.82	2.265	0.674	-0.999	1.67
			.40	---	---	---	---	---	.984	.435	-.971	1.44
			---	---	---	---	---	---	---	---	---	---
	AISI 316 stainless steel	---	.10	.0474	.189	e .996	.89	.80	---	---	---	---
			.27	.0009	1.415	(c)	---	---	---	---	---	---
			.40	---	---	---	---	---	4.118	.291	-.994	1.29
			.10	.038	.224	.993	1.00	.78	---	---	---	---
	AISI 318 A-286	---	---	.0202	.430	(c)	---	.57	---	---	---	---
			---	.0377	.181	e .997	---	.82	---	---	---	---
			---	---	---	---	---	---	---	---	---	---
			---	---	---	---	---	---	---	---	---	---
Inconel 600 Sicromo 9M (annealed)	Rene 41	---	---	.0055	.728	.999	---	.23	---	---	---	---
			---	.0138	.505	.996	---	.49	---	---	---	---
			---	---	---	---	---	---	---	---	---	---
			---	---	---	---	---	---	---	---	---	---
	Hastelloy X	---	---	---	---	---	---	---	---	---	---	---
			---	---	---	---	---	---	---	---	---	---
			---	---	---	---	---	---	---	---	---	---
			---	---	---	---	---	---	---	---	---	---
	Stellite 68 Sicromo 6M (hardened)	---	---	---	---	---	---	---	---	---	---	---
			---	---	---	---	---	---	---	---	---	---
			---	---	---	---	---	---	---	---	---	---
			---	---	---	---	---	---	---	---	---	---
L-605 Hastelloy X Sicromo 6M (annealed)	Mercury	149	0.10	0.0068	0.174	0.989	---	0.83	---	---	---	---
			---	.0174	.398	.999	---	.60	---	---	---	---
			---	---	---	---	---	---	---	---	---	---
			---	---	---	---	---	---	---	---	---	---
	---	---	---	.0182	.406	.997	---	.59	---	---	---	---
			---	.039	.473	.999	---	.53	---	---	---	---
			---	.098	.465	.982	---	.53	---	---	---	---
			---	---	---	---	---	---	---	---	---	---
	---	---	---	---	---	---	---	---	---	---	---	---
			---	---	---	---	---	---	---	---	---	---
			---	---	---	---	---	---	---	---	---	---
			---	---	---	---	---	---	---	---	---	---

^aCorrelations performed using mm³/min of average erosion rate and mm³ at cumulation erosion.^bValues to compute this ratio obtained from table III(a).^cDistant in cm between the horn and stationary specimen.^dOnly two data points available.^eOnly three data points available.

TABLE IV. - EROSION PARAMETERS OF DIFFERENT MATERIALS EXAMINED IN VARIOUS LIQUID IMPINGEMENT DEVICES

(a) Average and instantaneous erosion rates

Material	Device	Velocity, m/sec	Size (jet or drop), μm	Average erosion rate			Instantaneous erosion rate		
				Peak, ϵ_{ma} , mg/kg	Cumulative erosion at peak, V_{max} , mg/cm^2	Water impacted or number of impacts to attain the peak, t_{ma} , kg/cm^2	Peak, ϵ_{mi} , mg/kg	Cumulative erosion at peak, V_{mi} , mg/cm^2	Time to attain peak, t_{mi} , kg/cm^2
FV 566 stainless steel	EEC ^a	610	400	1488.00	253	0.17	1590.00	-----	-----
		530		828	149	.18	1000	-----	-----
	Napier ^b	427	↓	382	84	.22	460	-----	0.30
		314		119	152	1.28	193	-----	1.60
		329		47.40	287	6.05	92.80	-----	3.80
		311		640	41	6.05	92.80	-----	3.80
	CAPC	518	100	75	75	1	24.10	-----	1.08
		427		11	11	1	12.70	-----	2.56
		305		1.54	63	41	2.46	-----	22.40

Tool steel	EEC ^a	610	400	1290	258	0.20	2860	-----	-----
		530		880	176	.20	1330	-----	0.20
	Napier ^b	427	↓	286	80	.28	1000	-----	.40
		314		119	2.16	121	-----	2.50	-----
		311		-----	-----	-----	9.52	-----	2.60
		314		640	-----	-----	9.52	-----	2.60
	CAPC	518	100	3.10	185	59.70	2.03	-----	25.20

Stellite 6B	EEC ^a	610	400	681	124	0.18	910	-----	0.20
		530		398	191	.48	670	-----	.50
	CAPC	427	↓	138	126	.91	260	-----	1.04
		314		28.40	97	3.14	56	-----	385
		311		4.90	297	60.50	56	-----	385
		610		6.40	114	17.90	-----	-----	-----
	HSEM ^d	518	100	2.60	161	62	1.98	-----	28.90
		427		1.45	177	122	3.62	-----	69.50
		427		142	452	3.2	355	-----	1.30
		314		18.57	538	28.97	31.20	-----	15.50

Cobalt 18/8 stainless steel	Drop impact	125	1500	$e_{0.369 \times 10^{-3}}$	f_{273}	97.40×10^5	$e_{0.93 \times 10^{-3}}$	f_{150}	$h_{5.07 \times 10^5}$
				$e_{.890}$	f_{425}	94.78	$e_{2.86}$	f_{225}	$h_{3.50}$
Copper Mild steel 60/40 brass Silicon steel	↓	↓	↓	$e_{6.210}$	f_{233}	9.38	$e_{8.85}$	f_{166}	9.30
				$e_{1.740}$	f_{530}	93.05	$e_{2.93}$	f_{113}	91.25
				$e_{1.810}$	f_{681}	93.75	$e_{4.92}$	f_{461}	93.00
				$e_{1.520}$	f_{651}	94.28	$e_{4.33}$	f_{396}	93.50

^aEnglish Electric Company test rig.^bNapier rig (Central Electricity Generating Board, Marchwood).^cC.A. Parson's test rig.^dHigh-speed erosion machine (Central Electricity Generating Board, Marchwood).^eErosion rate, $\mu\text{m}/\text{impact}$.^fCumulative erosion at peak, μm .^gNumber of impacts corresponding to peak erosion rate.

TABLE IV. - Concluded. EROSION PARAMETERS OF DIFFERENT MATERIALS EXAMINED IN VARIOUS LIQUID-IMPINGEMENT DEVICES

(b) Power-law relation parameters

Material	Device	Velocity, m/sec	Size (jet or drop), μm	Power-law relation parameters									
				Acceleration zone, ^a $V/t = AV^n$					Deceleration zone, ^a $V/t = BV^{-m}$				
				A	n	R	$\epsilon_{ma}/\epsilon_{mi}$ (b)	(1 - n)	B	m	R	(1 + m)	
FV 566 stainless steel	EECC	610	400	-----	-----	-----	-----	-----	-----	-----	-----	-----	
		530		-----	-----	-----	-----	-----	-----	-----	-----	-----	
	Napier ^d	427	-----	-----	-----	-----	-----	-----	-----	-----	-----		
		314	-----	-----	-----	-----	-----	-----	-----	-----	-----		
	CAPE	329	640	-----	-----	-----	-----	-----	-----	-----	-----		
		311		-----	-----	-----	-----	-----	-----	-----	-----		
		518	100	-----	-----	-----	-----	-----	-----	-----	-----		
		427		-----	-----	-----	-----	-----	-----	-----	-----		
		305	-----	-----	-----	-----	-----	-----	-----	-----	-----		
				-----	-----	-----	-----	-----	-----	-----	-----		
Tool steel	EECC	610	400	-----	-----	-----	-----	-----	-----	-----	-----	-----	
		530		-----	-----	-----	-----	-----	-----	-----	-----	-----	
	Napier ^d	427	-----	-----	-----	-----	-----	-----	-----	-----	-----		
		314	2.652	0.648	0.998	-----	0.35	-----	-----	-----	-----		
	CAPE	311	640	.304	.549	.998	-----	.45	-----	-----	-----		
		314		.161	.633	.999	-----	.37	-----	-----	-----		
		518	-----	-----	-----	-----	-----	-----	-----	-----	-----		
				-----	-----	-----	-----	-----	-----	-----	-----		
Stellite 6B	EECC	610	400	-----	-----	-----	0.75	-----	17.830x10 ⁴	1.061	-0.995	2.06	
		530		20.550	0.604	-----	.59	0.40	174.400	1.538	-.999	2.54	
		427		3.609	.754	-----	.53	.25	12.660	1.351	-.992	2.35	
		314		1.409	.720	0.999	.51	.28	28.060x10 ²	.986	-.986	1.99	
	CAPE	311	100	.114	.702	.999	-----	.30	-----	-----	-----	-----	
		610		-----	-----	-----	-----	-----	-----	-----	-----	-----	
		518		-----	-----	-----	-----	-----	-----	-----	-----	-----	
		427		.499	.689	.998	.40	.31	60.240	.702	-.987	1.70	
	HSEM ^f	427	640	2.085	.742	.999	.40	.26	23.300x10 ³	.816	-.901	1.82	
		314		.387	.657	.998	.60	.34	-----	-----	-----	-----	
	Cobalt 18/8 stainless steel Copper Mild steel 60/40 brass Silicon steel	Drop impact ↓	125	1500	2.940x10 ⁻⁵	0.443	0.975	0.40	0.56	-----	-----	-----	-----
			6.320		.435	.952	.31	.56	1.968x10 ⁻²	0.516	-0.817	1.52	
			-----		-----	-----	.70	-----	40.730	1.368	-.954	1.37	
			2.560		.727	.998	.60	.27	-----	-----	-----	-----	
2.000			.706		.999	.37	.29	.119	.644	-.936	1.64		
1.920			.678		.996	.35	.32	.596	.915	-.893	1.92		

^aCorrelations were carried out using mm³/hr for average aerosion rate and mm³ for cumulative erosion.^bValues to compute this ratio obtained from table IV(a).^cEnglish Electric Company test rig.^dNapier rig (Central Electricity Generating Board, Marchwood).^eC.A. Parson's test rig.^fHigh-speed erosion machine (Central Electricity Generating Board, Marchwood).

TABLE V. - PARAMETRIC STUDY CALCULATION - STELLITE 6B EXAMINED

IN LIQUID-IMPINGEMENT DEVICE

[Correlations carried out using EEC data at different velocities.

Units of ϵ_{ma} and ϵ_{mi} are mg/kg.]

Least-squares-fit equation	Correlation coefficient
Peak average erosion rate, $\epsilon_{ma} = 2.18 \times 10^{-11} (\text{velocity})^{4.86}$	0.999
Peak instantaneous erosion rate, $\epsilon_{mi} = 1.11 \times 10^{-9} (\text{velocity})^{4.30}$.993
Coefficient, $A = 4.03 \times 10^{-13} (\text{velocity})^{4.99}$.964
Coefficient, $B = 4.93 \times 10^{-16} (\text{velocity})^{7.64}$.828

1. Report No. NASA TP-2339		2. Government Accession No.		3. Recipient's Catalog No.	
4. Title and Subtitle Empirical Relations for Cavitation and Liquid Impingement Erosion Processes				5. Report Date August 1984	
				6. Performing Organization Code 506-53-1B	
7. Author(s) P. Veerabhadra Rao and Donald H. Buckley				8. Performing Organization Report No. E-1872	
				10. Work Unit No.	
9. Performing Organization Name and Address National Aeronautics and Space Administration Lewis Research Center Cleveland, Ohio 44135				11. Contract or Grant No.	
				13. Type of Report and Period Covered Technical Paper	
12. Sponsoring Agency Name and Address National Aeronautics and Space Administration Washington, D.C. 20546				14. Sponsoring Agency Code	
15. Supplementary Notes P. Veerabhadra Rao, NASA Lewis Research Center Resident Research Associate and Cleveland State University, Cleveland, Ohio (work done under NASA cooperative agreement NCC3-21); Donald H. Buckley, Lewis Research Center. Published in part in the International Journal of Mechanical Sciences, 1984, as paper entitled A Unified Relation for Cavitation Erosion.					
16. Abstract A unified power-law relationship between average erosion rate and cumulative erosion is presented. Extensive data analyses from venturi, magnetostriction (stationary and oscillating specimens), liquid drop, and jet impact devices appear to conform to this relation. A normalization technique using cavitation and liquid impingement erosion data is also presented to facilitate prediction. Attempts are made to understand the relationship between the coefficients in the power-law relationships and the material properties.					
17. Key Words (Suggested by Author(s)) Erosion; Prediction; Long-term operation; Cavitation; Liquid impingement; Empirical equations				18. Distribution Statement Unclassified - unlimited STAR Category 26	
19. Security Classif. (of this report) Unclassified		20. Security Classif. (of this page) Unclassified		21. No. of pages 27	
				22. Price* A03	

National Aeronautics and
Space Administration

Washington, D.C.
20546

Official Business

Penalty for Private Use, \$300

THIRD-CLASS BULK RATE

Postage and Fees Paid
National Aeronautics and
Space Administration
NASA-451



NASA

POSTMASTER: If Undeliverable (Section 158
Postal Manual) Do Not Return
